Transient porosity during fluid-mineral interaction. Part 1: In-situ 4D tomography

Hamed Amiri[1], Vangelis Dialeismas[1], Damien Freitas[2], Roberto Rizzo[1], Alireza Chogani[1], Christian M. Schlepütz[3], Florian Fusseis[4,5], Oliver Plümper[1,6]

[1]Department of Earth Sciences, Utrecht University, Utrecht, the Netherlands
[2]The University of Manchester at Harwell, Diamond Light Source, Harwell Campus, Didcot, OX11 0DE, UK
[3]Swiss Light Source, Paul Scherrer Institut, Forschungsstrasse 111, 5232 Villigen PSI, Switzerland
[4]School of Geosciences, University of Edinburgh, United Kingdom
[5]Applied Structural Geology, RWTH-Aachen University, Aachen, Germany
[6]Faculty of Geosciences and MARUM - Center for Marine Environmental Sciences, University of Bremen, Bremen, Germany

Key Points:

- Operando X-ray synchrotron tomography of salt replacement enables observation and quantification of reaction-induced porosity evolution.
- A set of statistical descriptors and Minkowski functionals quantitatively capture the dynamics of pore structure and morphology.
- Analysis reveals a three-stage pore evolution including rapid evolution, transition, and steady state.

Corresponding author: Hamed Amiri, `h.amiri@uu.nl`

Abstract

Fluid-induced mineral replacement reactions play a key role in controlling porosity generation and permeability evolution in geologic systems. However, the dynamic feedback between pore structure development and fluid transport remains poorly quantified. This study investigates the spatiotemporal evolution of reaction-induced pore space in the fluid-driven KBr–KCl system using time-resolved synchrotron X-ray tomography. Due to its high solubility and rapid reaction kinetics, the KBr–KCl system serves as an effective analogue for fluid–rock interactions in natural settings. We performed two *operando* experiments at the TOMCAT beamline (Swiss Light Source): one with direct KCl solution flow over a KBr crystal, and another using a pressurized X-ray-transparent cell. Machine-learning-based segmentation enabled quantitative analysis of porosity evolution through spatiotemporal correlation functions and transport property estimation. We identified a three-stage pore evolution process: (1) rapid pore channel formation along crystallographic axes with high reaction rates and a rough interface; (2) a transitional stage characterised by smoother interfaces and enhanced lateral connectivity; and (3) a steady-state regime where permeability continues to increase due to pore coarsening and reduced tortuosity. These results advance our quantitative understanding of how reaction-induced porosity governs dynamic fluid–rock interactions.

Plain Language Summary

Understanding how rocks change when they come into contact with fluids is important for many natural and industrial processes, such as groundwater flow, carbon storage, and resource extraction. These interactions create small voids called pores, which are critical because they form the pathways that allow fluids to move through rocks and influence large underground regions. In this study, we used a simple salt-based system to mimic these fluid-rock interactions and explore how pores form and evolve over time. We used high-resolution X-ray imaging to observe the process in real time and applied artificial intelligence and mathematical tools to analyse how the pore structure changed during the reaction. Our findings show that pore formation is a complex, dynamic process that occurs in three stages: an initial rapid change, a transitional phase, and a final stable state. Each stage affects the ease with which fluids can move through the material in different ways. By revealing how the structure of the pores influences fluid flow, our study improves our quantitative understanding of natural systems.

1 Introduction

Geological processes that alter and transform rocks in the presence of aqueous fluids are fundamental in determining Earth's dynamics. Such fluid-driven mineral transformations occur across a wide range of settings and scales. They also address a wide range of societal challenges, such as resource management, climate change mitigation, and environmental remediation. These fluid-rock interactions shape the Earth's crust and mantle by influencing surface features, geochemical cycles, and the properties of subsurface environments. A critical aspect of such transformations is the creation of fluid pathways through mineral replacement reactions, a phenomenon essential for large-scale rock alteration and mass transport. For example, serpentinization of the oceanic mantle produces hydrogen gas that sustains subsurface microbial ecosystems (e.g,. Bach et al., 2006; Malvoisin et al., 2021; Plümper et al., 2012). Similarly, albitization of crustal igneous rocks alters fluid chemistry in the Earth's crust (e.g., Engvik et al., 2008; Kaur et al., 2012; Norberg et al., 2011). Another example is the eclogitization of subducted oceanic materials, which influences metamorphic processes in subduction zones (e.g., Angiboust et al., 2014; Pollok et al., 2008). Alteration of carbonate-bearing sedimentary systems likewise impacts the global carbon cycle (e.g., Weber et al., 2023).

In addition to their geologic importance, fluid-driven mineral transformations are crucial for various applications. They play a role in the fractionation of rare-earth elements and in the sequestration of radionuclides or heavy metals (e.g., Julia et al., 2023), and contribute to carbon dioxide storage through mineral carbonation (binding CO_2 as stable mineral phases, e.g., Kelemen & Matter, 2008), alongside direct precipitation mechanisms. In all these cases, fluid–rock reactions at the mineral scale require the development and maintenance of pore networks and permeability at grain boundaries (e.g., Plümper et al., 2017a; A. Putnis, 2015). This interconnected porosity is what allows fluids to continuously circulate through and react with rocks that would otherwise be essentially impermeable.

One fundamental mechanism that enables these fluid–rock transformations is fluid-induced mineral replacement. In this prevalent physicochemical process, a parent mineral comes into contact with a chemically reactive fluid (one out of equilibrium with the mineral), leading to dissolution of the parent mineral and simultaneous precipitation of a new, more stable product phase. This coupled dissolution–precipitation mechanism is often referred to as interface-coupled dissolution–precipitation (ICDP). It can result in pseudomorphic replacement, in which the newly formed mineral retains the external shape and volume of the original parent mineral (e.g., C. V. Putnis & Mezger, 2004; A. Putnis, 2009). A key feature of fluid-induced replacement reactions is the generation of porosity at the reaction interface. Differences in molar volume and relative solubility between the parent and product phases typically create reaction-induced porosity in the product phase. For instance, if the parent phase is more soluble in the fluid than the product phase, it will dissolve away faster than the product can precipitate, leaving behind extra pore space within the product matrix. This process yields a porous, interconnected reaction front through which the fluid can infiltrate. The presence of a fluid-filled pore network at the interface is crucial: it provides pathways for the reactant fluid to penetrate and sustain the reaction progress deeper into the material. However, this porosity is often transient (e.g., A. Putnis, 2015). As the reaction proceeds, ongoing precipitation of the product mineral can partially clog pores or reduce their connectivity, even as continued dissolution elsewhere may open new pore space. The evolving balance between dissolution and precipitation strongly influences the rock's changing properties, reflecting a competition between reaction kinetics and the transport of reactants through the transient pore network (e.g., Koehn et al., 2021). In particular, transient porosity and its connectivity control the system's permeability, and they can also affect the mechanical and rheological characteristics of the rock (e.g., Gardner et al., 2021; Yarushina et al., 2025).

Numerous experimental studies have examined these mineral replacement processes to better understand how porosity develops. Examples include the transformation of aragonite to calcite (Perdikouri et al., 2011), calcite to fluorite (Pedrosa et al., 2016a), and carbonate to apatite (Kasioptas et al., 2008), among others. One model system that has been especially well studied for such reactions is the KBr–KCl halite replacement. This system is advantageous for research because the reaction completes rapidly and the salts involved are highly soluble (C. V. Putnis & Mezger, 2004; C. V. Putnis et al., 2005). In a typical experiment, a single crystal of potassium bromide (KBr) is immersed in a potassium chloride (KCl) solution. Chemically, the transformation follows the reaction:

$$KBr_{(s)} + Cl^-_{(aq)} \leftrightarrow KCl_{(S)} + Br^-_{(aq)} \tag{1}$$

where (s) and (aq) denote solid and aqueous phases, respectively. When a KBr crystal comes into contact with a saturated KCl solution, dissolution begins at the crystal's surface. As this occurs, the local solution at the crystal-fluid interface becomes enriched with Br until the interfacial fluid is saturated with respect to a K(Br,Cl) solid solution, leading to the simultaneous recrystallisation of a new phase which is only temporarily in equilibrium with the solution composition, as further Cl is transported from the KCl source, making this equilibrium composition richer in the Cl. The composition of the product phase continually

adjusts towards the KCl end-member as long as the reaction advances (C. V. Putnis & Mezger, 2004).

The development of porosity in this reaction system arises from both thermodynamic and kinetic factors. Thermodynamically, KBr is more soluble than KCl, so the fluid at the interface becomes undersaturated with respect to KBr but supersaturated with respect to a K(Br,Cl) solid solution. Therefore, more KBr is dissolved into the solution, which together with its larger molar volume than the product phase (i.e., negative volume change), leads to generating pores. Kinetically, dissolution of KBr proceeds more rapidly than precipitation of the product phase, leading to a transient imbalance that produces reaction-induced porosity within the growing rim. The advance of the reaction front is then controlled by the transport of Cl and Br through this porous product layer (e.g., C. V. Putnis & Mezger, 2004; C. V. Putnis et al., 2005; A. Putnis, 2009).

The result is a porous reaction rim of a new material that envelops the unreacted KBr core. This porous rim is permeable, allowing the external KCl solution to seep inward through the product phase. As a consequence, the reactive fluid can reach the unreacted KBr interface just beneath the rim, and the replacement reaction can progress from the outside of the crystal toward its interior. Over time, distinctive pore structures develop in the KBr–KCl system. The product rim initially contains a high density of small, interconnected pores, which maintain effective fluid pathways to the reaction front. Within the dissolving KBr core just behind the advancing interface, narrow cylindrical pores begin to form and tunnel inward. These pore channels, often described as "finger-like" or filamentary pores, propagate from the reaction front into the unreacted KBr (e.g., Kar et al., 2015, 2016). In addition to these finger pores, disk-shaped cavities have been observed parallel to the reaction interface (Raufaste et al., 2011). The finger-like pores essentially function as dead-end channels: they open at the reactive interface but do not immediately connect through to the far side of the crystal. However, in the early to mid stages of the reaction, these channels remain filled with fluid and remain connected to the external solution via the porous rim. This architecture ensures that fresh reactant fluid can continuously access new KBr surfaces along the growing fingers, allowing the dissolution–precipitation reaction to proceed deeper into the crystal. Ultimately, KBr can be completely replaced by the KCl-rich product if fluid access is maintained. As the reaction approaches completion, some of the pore channels may widen (coarsen) or become partially clogged by late-stage precipitates, which can reduce overall porosity and permeability (Beaudoin et al., 2018). However, by that stage, the bulk of the replacement is already achieved, underscoring how crucial the earlier presence of open, connected pores is for full conversion of the crystal.

Fluid flow within these dead-end microscale pores is notable because it may not align with standard Darcy's law expectations for flow through porous media. Kar et al. (2015, 2016) proposed that in the KBr–KCl system, ion concentration gradients developing inside isolated pore channels can induce diffusio-osmotic flow. In simple terms, as KBr dissolves, a high concentration of ions builds up at the closed end of a finger pore. This imbalance in ion concentrations between the pore interior and the bulk solution can generate a fluid flow from the high-concentration region to the low-concentration region, effectively pushing fluid out of the dead-end pore. The movement of charged ions in turn sets up local electric fields, which drive an electro-osmotic flow of fluid along the charged pore walls. Together, these coupled diffusio-osmotic and electro-osmotic effects self-propel the fluid within the finger-like pores, circulating fresh solution in and out of what would otherwise be stagnant cul-de-sacs. This phenomenon helps to keep the reaction interface supplied with reactants and removes dissolved products, thereby accelerating the replacement process beyond what simple diffusion would accomplish. Significantly, Beaudoin et al. (2018) directly observed the development of these finger-shaped pore channels using 3D X-ray microtomography. Their imaging confirmed that the pores form elongated channels that advance into the unreacted crystal and that these channels enhance the reactive surface area. The presence of such finger pores effectively enlarges the reactive zone and maintains fluid flow at the reaction

front, promoting a more extensive and faster mineral replacement than would occur in their absence.

Interestingly, the formation of channel-like pores during mineral replacements is not unique to the KBr–KCl system. Similar wormhole or channel structures have been observed in other laboratory and natural settings. For example, Pedrosa et al. (2016b) observed that when marble (a carbonate rock) is replaced by apatite, the reaction produces elongated pore channels in the product phase. Likewise, the replacement of calcite with fluorite in experimental studies was found to create channelised porosity (Pedrosa et al., 2016a), analogous to finger pores in halite experiments. The dolomitization process (replacing calcium carbonate with dolomite in sedimentary rocks) also shows evidence of rhythmic channel-like porosity forming as the reaction front advances, even under static or diffusion-dominated fluid conditions (e.g., Kondratiuk et al., 2015, 2017; Weber et al., 2021, 2023; Lefeuvre et al., 2024). Researchers have even proposed that analogous microscale fluid pathways develop during feldspar alteration in the Earth's crust (e.g., Plümper et al., 2017b, 2017c). In such scenarios, reaction-induced pore networks could dramatically enhance fluid circulation in crystalline rocks, potentially governing large-scale fluid flow in the lithosphere without the aid of fractures or tectonic pumping. Together, these observations suggest that reaction-induced porosity and its associated fluid flow are a general mechanism by which fluids can permeate and alter rocks that would otherwise be nearly impermeable. This mechanism appears to operate independently of external stress or rock deformation, which means that the chemical reactions themselves create the permeability necessary for fluid transport.

Although past studies have greatly improved our understanding of interface-coupled dissolution–precipitation and the evolution of reaction-induced porosity, there are still significant knowledge gaps due to experimental limitations. Many analyses have relied on 2D imaging techniques (such as scanning electron microscopy on cross-sections) to infer pore structures. However, these 2D snapshots cannot capture the 3D connectivity of pores or how they evolve over time. Other studies have used X-ray tomography to observe 3D pore structures, but these were often discontinuous 3D observations or stop-motion observations (Beaudoin et al., 2018). More recently, pseudo-4D approaches have been applied to mineral replacement reactions, such as dolomitization (Lefeuvre et al., 2024). In such experiments, multiple identical samples are reacted for different durations, and each is imaged once, providing a series of static 3D views at coarse time intervals. This approach can miss important transient stages of the development of pore networks and can introduce inconsistencies: because each sample may have slight differences in initial conditions or reaction progress, the sequence of images might not perfectly represent the true progression in a single sample. In short, previous experimental methods have rarely captured a continuous 3D timeline of how pores nucleate, grow, and connect during mineral replacement. More importantly, such a discontinuous approach requires removing the sample from the reacting solution for each scan. This external perturbation can alter local reaction conditions, including inducing transient surface precipitation that partially obstructs fluid access and modifies the natural evolution of the pore network. Furthermore, most previous studies emphasise the measurement of total porosity or making qualitative observations about the shape of the pores, rather than quantitatively tracking the morphological evolution of the pore network. As a result, dynamic processes, for example, the rate at which pores coalesce or how pore connectivity changes at different reaction stages, remain poorly understood. This lack of detailed temporal data makes it challenging to fully explain the relationship between reactive fluid flow and evolving transport properties in reactive systems.

In this study, we overcome these limitations by using 4D synchrotron X-ray tomography – that is, three-dimensional imaging over time – to directly observe the fluid-driven KBr–KCl replacement reaction in unprecedented detail. This time-resolved 3D imaging technique allows us to visualise how the pore network develops and changes almost continuously as the reaction proceeds without any external perturbations. We capture a high-resolution

3D image series of the same sample throughout the experiment, effectively watching the reaction-induced porosity form and transform in real time. To analyse a large amount of image data, we employ a combination of advanced techniques. First, we used deep learning-based image processing to segment the tomography data, ensuring that pores and solid phases are accurately identified at each time step. We then quantify the microstructural evolution using statistical microstructure descriptors (SMDs) (Jiao et al., 2007; Chen et al., 2019, 2022) and Minkowski functionals (MFs) (Mecke, 2000). These mathematical tools enable a comprehensive characterisation of the pore space geometry, connectivity, and morphology as the reaction progresses. Through this interdisciplinary approach, we can measure changes in structural and morphological properties of pores frame-by-frame during the experiment. Our results reveal intricate interactions between the chemical reaction kinetics, the resulting pore structure, and the pathways available for fluid flow. By quantitatively linking the evolution of the pore geometry with transient transport properties, we shed light on how local permeability and fluid flow patterns emerge and change during mineral replacement. In general, this work provides a more quantitative and dynamic understanding of how reaction-induced porosity develops, how it sustains fluid circulation in low-permeability environments, and how these processes feed back into the efficiency and extent of fluid-driven rock transformations.

2 Methodology

2.1 Experimental setup

Previous studies of KBr-KCl replacement have used 2D or 3D imaging techniques to investigate the ICDP mechanism and assess the evolution of reaction-induced porosity. However, recent advances in synchrotron facilities, computational resources, and data storage have allowed the addition of time to 3D μ -CT, allowing time-resolved imaging at high resolution (Marone et al., 2020). This technological breakthrough offers an unprecedented opportunity to study the microstructural evolution and characterise various physical properties of rocks in real time (Noiriel & Renard, 2022).

Time-resolved (4D) synchrotron tomography datasets were acquired during the experiments at the Swiss Light Source (SLS) TOMCAT beamline, using a filtered white beam with an energy peak at 27 keV. For each μ-CT dataset, 2000 radiographs were collected over 180° rotation with an angular step of 0.09° and exposure time of 1 ms. The resulting radiographs had an effective voxel size of 2.75 μm, from which 3D μ-CT datasets with dimensions of 2016 voxels × 1584 voxels × 1584 voxels were reconstructed using a fast Fourier method (Marone et al., 2017). This method effectively reduces common ring artefacts, allowing for continuous observation of the reaction's progression during image collection. The frequency rate of the tomoscopy was set at 10 s, with approximately 1-minute intervals between successive scans. Using this setup, several operando KBr-KCl replacement experiments were conducted with different configurations. KBr crystals from Alkor Optics, measuring 3.175 mm in diameter and 5 mm in height, were used.

Here, we focus on two experiments. In the first experiment (Exp 1), KCl fluid was introduced onto the KBr crystal at 0.05 ml/min while simultaneously performing X-ray scanning (Figure 1a). In the second experiment (Exp 2), the crystal was placed in the Sleipnir cell (Fusseis et al., 2014), with KCl fluid introduced through a 1 mm diameter hole at the centre (Figure 1b). The sample was pressurised to 10 bar using remote-controlled syringe pumps, and both experiments were conducted at ambient temperature. Sleipnir is a hydraulic, X-ray translucent apparatus designed to perform fluid flow experiments on samples under confining pressure. The sample and pore fluid line are isolated from the confining deionised water (DI water) by an elastomeric silicone jacket. High pressure is generated using Cetoni high-pressure syringe pumps, allowing fine control over the confining pressure, pore fluid pressure, and fluid injection rate in the sample inlet.

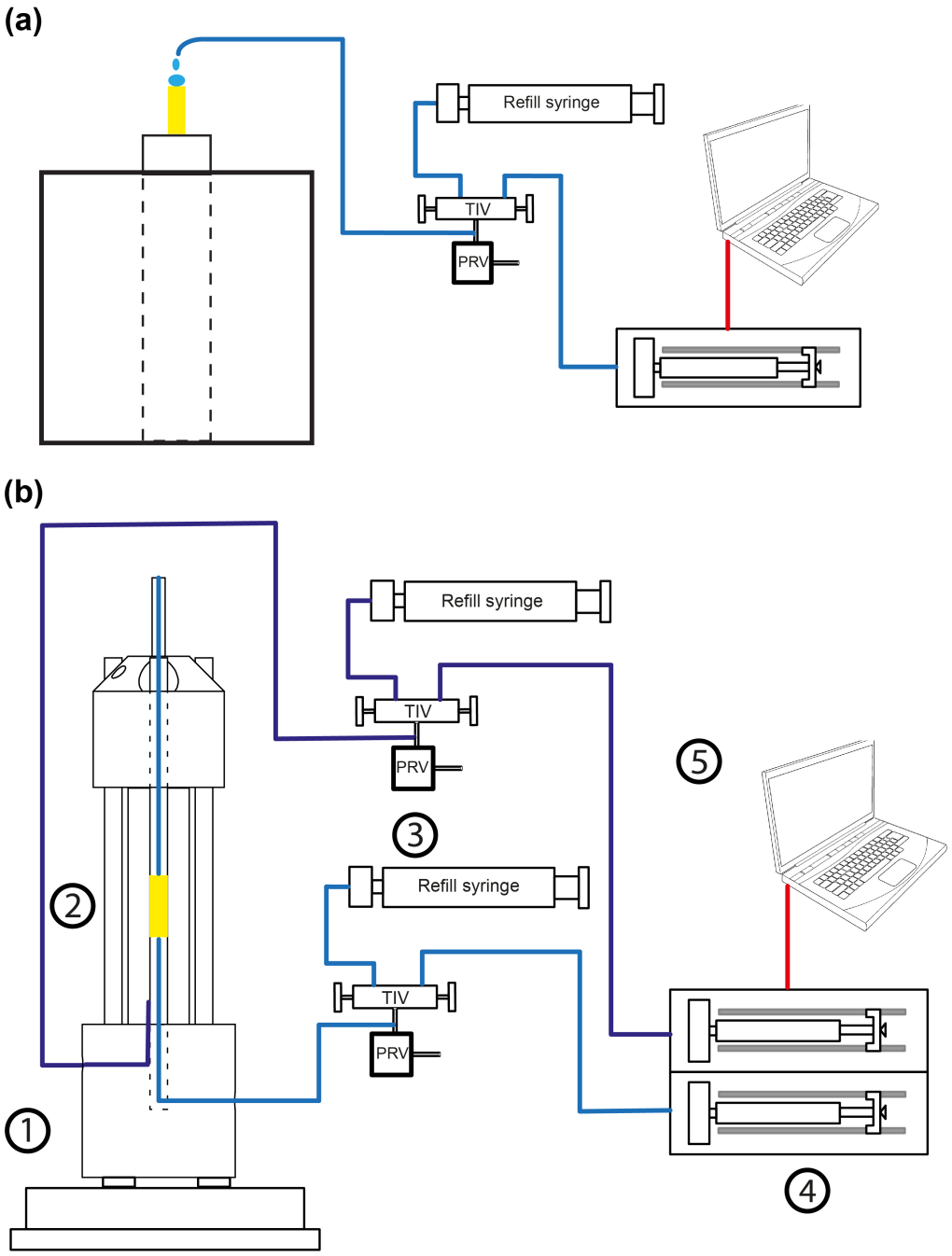

Figure 1. Experimental setups for both configurations. (a) Setup for Exp 1, where KCl solution droplets were delivered onto the surface of a KBr crystal (yellow rectangle). (b) Setup for Exp 2, consisting of the Sleipnir cell (1) where the KBr crystal (2, yellow rectangle) was enclosed, and the KCl fluid was injected through a hole at the bottom of the sample. The experimental system includes manifolds equipped with refill syringes, pressure relief valves (PRV), and top industry valves (TIV) (3). Cetoni high-pressure syringe pumps (4) controlled the fluid flow, with the system monitored and regulated via a laptop interface (5). For more details on individual components, refer to Fusseis et al. (2014).

Figure 2 illustrates the evolution of reaction-induced pores in both experiments within selected regions of interest (ROIs). In Exp 1, the ROI was chosen at a distance from the upper part of the sample centre for two reasons: (1) the crystal dissolved completely at the top over time and (2) the air infiltrated from the edges after some time, visible as black pixels in the greyscale images in Figure S1a. This ROI encompassed 266 slices, each measuring 512^2 pixels, with physical dimensions of $731.5 \times 1408 \times 1408$ μm, and a total volume of 1.45 mm^3 (Figure 2a). In Exp 2, the ROI consisted of 251 slices, each measuring 200^2 pixels, corresponding to physical dimensions of $690.25 \times 550 \times 550$ μm and a total volume of 0.21 mm^3 (Figure 2b). The smaller ROI here was chosen due to the collapse of the sample jacket after 75 minutes, which damaged much of the lower part of the sample, as discussed later (see Figure 6a). Supplementary Videos S1 and S2 show the 3D time-lapse evolution of pore space in Exp 1 and Exp 2, respectively.

The acquired images were segmented using a combination of supervised machine-learning (random forest classifier) and deep-learning approaches based on a U-Net convolutional neural networks (CNNs). The machine learning model was trained on representative manually annotated slices using pixel classification workflow implemented in the ilastik software (Berg et al., 2019). This trained model was subsequently employed to segment 3% of all images. These segmented images were then used as labelled training images, together with the corresponding greyscale images, to train a CNN with a U-Net architecture (Ronneberger et al., 2015). The trained CNN was finally used to segment all the images. More details on the segmentation methods and representative segmented images are provided in the Supplementary Information (Text S1 and Figure S1).

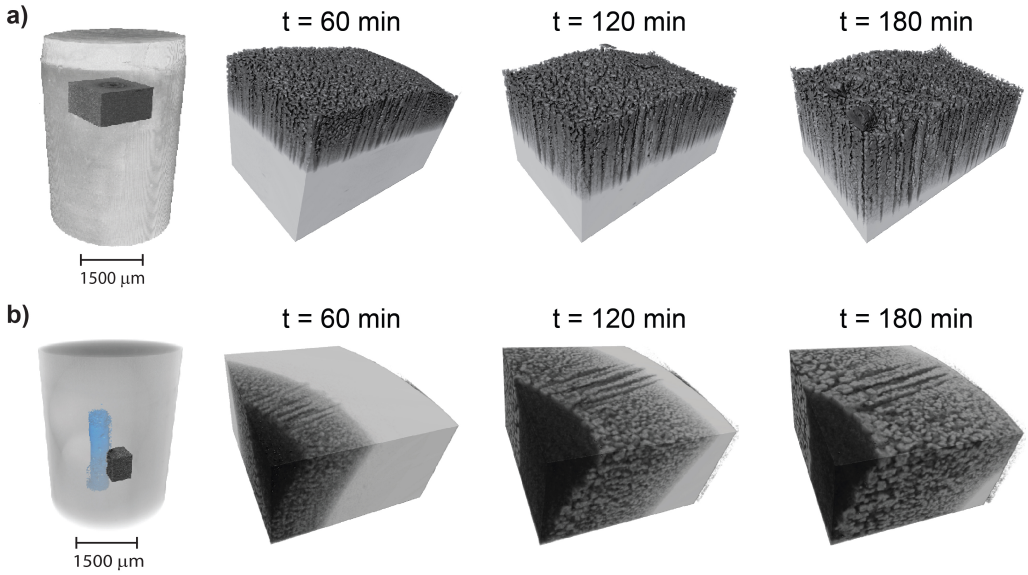

Figure 2. Snapshots of 3D scans were acquired from both experiments at different times. (a) Evolution of the reaction and the induced porosity in Exp 1, where KCl fluid was introduced on top of the KBr crystal, as shown in Figure 1a. (b) Development of reaction-induced porosity in Exp 2, where the fluid is injected into the cell from a central hole at the bottom (Figure 1b). The ROI in Exp 2 was selected from the bottom of the sample around the central hole highlighted in blue (see also Figure 6a). The leftmost images show the scans at the beginning of the experiments, with the dark grey volume representing the ROI in each experiment.

2.2 Statistical microstructure descriptors

Statistical microstructure descriptors (SMDs) are statistical tools used to quantify the structural and morphological properties of a material's microstructure. This statistical characterisation provides a quantitative understanding of microstructures, which, in turn, controls the physical properties of rocks across various scales. Among the most common statistical descriptors are spatial correlation functions, also known as n-point correlation functions. These are defined as the probability that n random points with specific configurations occur within the phase of interest, such as pores in rocks. They are computed by sampling processed images (i.e., segmented images where each phase is labelled) with a set of predefined query points (Bostanabad et al., 2018).

One of the simplest and most widely used descriptors is the two-point correlation function, S_2, which measures the probability that two random points separated by a distance r lie within the same phase (Torquato & Haslach, 2002). While S_2 effectively quantifies the microstructure of certain single-scale rocks, such as sandstone (Jiao et al., 2008), higher-order correlation functions (i.e., $n >= 3$) are necessary for accurately characterising complex heterogeneous rocks. However, obtaining these higher-order functions is computationally expensive, as it necessitates considering all possible point configurations in an image. To address this limitation, Chen et al. (2019) introduced n-point *polytope* functions, P_n, which calculate the probability of n vertices of regular polygons with an edge length of r. Polytope functions can be considered a subset of n-point correlation functions, where points lie at vertices of specific polygons such as triangles, squares, and hexagons. Successively incorporating these higher-order correlation functions allows us to encode geometrical patterns in the microstructure in an accurate, explainable, and computationally efficient way.

Additionally, to quantify the connectivity of the pores generated during the KBr-KCl reaction, we use the *lineal-path* function L (Lu & Torquato, 1992) and the *two-point cluster* function C_2 (Jiao et al., 2009). The lineal-path function, $L(r)$, computes the probability that an entire line of length r lies within the same phase, providing insight into the linear connectivity within the microstructure. The cluster function, $C_2(r)$, is similar to S_2, but with the requirement that the two random points lie within the same connected cluster of the phase.

Figure 3a illustrates scenarios in which two random points, n vertices of different polygons, or a whole line segment land within the pore space. Figure 3b provides an example of quantification using these SMDs, providing information on the structural properties of the microstructure. Initially, all SMDs start from the same probability corresponding to the porosity, since the above definitions reduce the probability of finding a single random point in the pore space. These curves then decay quickly at small r values, giving information about small-scale features such as pore size and interaction between pores. For example, the average pore size can be approximated from the r value at the first minimum value in S_2. A bump in the long range indicates a spatial correlation between the pores. In addition, the r at which L drops to zero indicates the length of the most elongated pore in the image, which in this example is 85 pixels (or 234 μm, given the pixel size of 2.75 μm). However, the higher probability of C_2 compared to L demonstrates that cluster connectivity is dominant.

Furthermore, we compute the average chord length, $\bar{l_c}$, which is defined as the average length of line segments (chords) that travel through pores before hitting the pore-solid interface. This parameter provides an average measure of the pore size and can be estimated from S_2 (Torquato & Haslach, 2002):

$$\bar{l_c} = \frac{S_2(0)}{S_2'(0)} \tag{2}$$

where $S_2'(0)$ is the derivative of S_2 at $r = 0$. This calculation is equivalent to determining the intersection of the line fitted to the S_2 curve at the origin with the r-axis, as illustrated in

Figure 3b. In this example, the fitted line intersects the r-axis at $r = 12$ pixels, corresponding to an average chord length of approximately 33 μm.

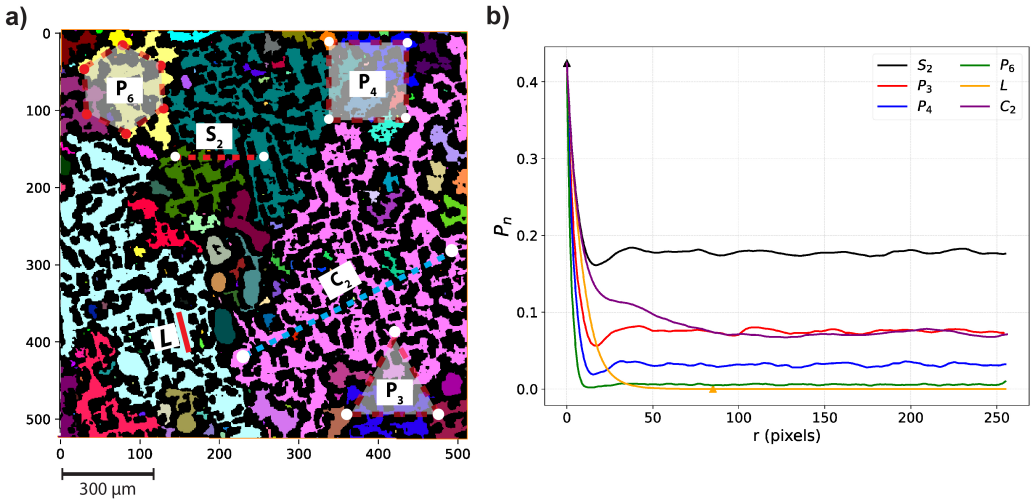

Figure 3. An example of characterisation of a microstructure image using SMDs. (a) Visual illustration of SMDs on a segmented image from the experiments. Each colour represents a connected group of pixels, while black pixels show a solid phase. (b) Results of microstructure quantification using SMDs. The triangle marker at $r = 0$ represents the phase fraction (porosity), while the orange one shows the r at which lineal path becomes zero, indicating the size of the largest linear pore in the image.

Although this set of SMDs enables an accurate microstructure characterisation, it is crucial to capture the structural features that emerge during the experiments. To quantify the evolution of reaction-induced porosity, we employ a time-dependent metric, Ω_n, introduced by Chen et al. (2022). This metric calculates the $L1$ distance between SMDs computed from the microstructure at time t and a reference time t_0:

$$\Omega_n(t) = \frac{1}{N}\sum_{r=0}^{L} |SMD(r;t) - SMD(r;t_0)| \tag{3}$$

Here, r represents the distance between points for S_2 and C_2, the length of the line segment for the lineal path function, or the edge length for n-point polytope functions, computed up to the largest distance L. Furthermore, N denotes the number of SMDs captured at different distances r. It is important to note that $\Omega_n(t)$ in Equation 3 can be used to calculate the distance between any two-time steps in an evolving system, such as between two consecutive snapshots of the microstructure. This versatility allows us to quantify the evolution of the pore space in terms of geometrical patterns and linear and cluster connectivity.

Physically, Ω_n provides a measure of the magnitude of microstructural change between two states. Large values of Ω_n indicate substantial reorganization of the pore network, such as rapid pore generation, growth, coalescence, or changes in connectivity across multiple distances. Conversely, small Ω_n values reflect limited structural change, consistent with incremental evolution or near steady-state behaviour. In this sense, Ω_n does not describe an absolute property of the microstructure, but rather quantifies how strongly the pore structure and morphology evolve over time.

Although SMDs provide valuable information on microstructures, establishing a clear relationship between their evolution and changes in the physical properties of rocks is not straightforward. One reason is that the resulting values of the Ω metric depend on the reference image, which means that this metric primarily quantifies the magnitude of changes in the microstructure. Additionally, evaluating these SMDs in 3D is computationally expensive. Therefore, more efficient computational tools are needed to accurately quantify the key properties of the complex pore space in 3D. One such efficient approach involves using Minkowski functionals, which we discuss in the next section.

2.3 Minkowski functionals

Minkowski functionals (MFs) are morphological measures that are used to describe materials with complex structures. Initially introduced in integral geometry (Mecke, 1998, 2000), MFs are effective and robust tools for characterising porous media through image processing techniques and establishing the relationships between morphological and physical properties of porous media (Mecke & Arns, 2005; Vogel et al., 2010; Mosser et al., 2017). For a 3D body Y with a smooth boundary δY, four MFs can be calculated from binary images: volume (V), surface area (S), integral mean curvature (M), and Euler characteristic (χ) of the pore space. These functionals are calculated using QuantImPy python package (Boelens & Tchelepi, 2021) and are defined by the following equations:

$$V = \int_Y dv \tag{4}$$

$$S = \int_{\delta Y} ds \tag{5}$$

$$M = \frac{1}{2} \int_{\delta Y} \left[\frac{1}{R_1} + \frac{1}{R_2} \right] ds \tag{6}$$

$$\chi = \frac{1}{4\pi} \int_{\delta Y} \left[\frac{1}{R_1 R_2} \right] ds = N_{vertices} - N_{edges} + N_{faces} - N_{volumes} \tag{7}$$

Here, ds is a surface element, and R_1 and R_2 represent the minimum and maximum radius of the surface curvature of the pore-solid interface, which are positive for convex and negative for concave curvatures. For a 3D binary image, instead of evaluating the integral in Equation 7, the Euler number can be efficiently calculated by decomposing the pore space into voxels and counting the number of vertices ($N_{vertices}$), edges (N_{edges}), faces (N_{faces}), and volumes ($N_{volumes}$) (Vogel et al., 2010). The Euler characteristic provides a morphological description of the connectivity of the pore space. According to the right side of Equation 7, for a pore space with mainly isolated pores, an increase in $N_{vertices}$ and N_{faces} leads to a larger positive value. In contrast, the number of edges increases in a well-connected pore space, resulting in a more negative value for the Euler characteristics. Normalising these measures by the total volume of the sample (i.e., image volume) yields porosity, specific surface area (S_v), specific integral mean curvature of pore surface (M_v), and specific Euler characteristics (χ_V), respectively. This normalisation facilitates the comparison of these properties across experiments with different sample volumes.

3 Results

3.1 Quantifying microstructure evolution

To quantify the evolution of the microstructure, we calculated Ω_n in various time steps from the beginning of the experiment (t=0). Figure 4a illustrates the evolution of the pores in a slice of Exp 1 in the XY plane, that is, from the top view of Figure 2a. The dynamics of the evolving pore space was quantified by calculating Ω_n for the SMDs at different times. As shown in Figure 5a, Ω_n for all SMDs increases when the reaction reaches the selected slice (i.e., about 110 minutes) until 140 minutes, with S_2 exhibiting the fastest evolution. After 140 minutes, all SMDs reach a plateau and stabilise, suggesting that the microstructure does not undergo significant changes in structural and geometrical patterns beyond this point. However, C_2 continues to increase with some fluctuations until the end of the experiment. These microstructural interpretations can be visually corroborated in Figure 4a, where the pores are more connected at 180 minutes compared to 140 minutes.

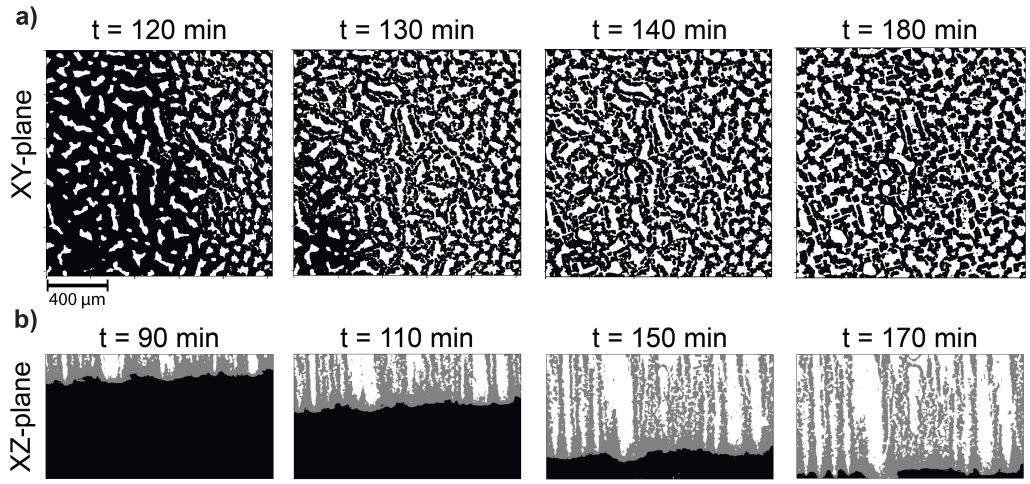

Figure 4. Snapshots of pore space at different times in Exp 1. (a) Evolution of porosity in a slice selected from the XY plane perpendicular to the channel-shape pores. White and black pixels represent pores and other phases, respectively. (b) Evolution of pores in the XZ plane where reaction-induced channels propagate downwards. Here, three phases were segmented: generated pores (white), reacted zone (gray), and KBr crystal (black).

Figure 4b displays the dynamics of the microstructure in the XZ plane, which is parallel to the direction of the propagated channels shown in Figure 2a. In this example, three phases including pores (white), reacted zone (grey) and non-reacted KBr crystal (black) were segmented to track the reaction front and compute its velocity, as presented in the next section. Ω_n metrics shown in Figure 5b indicate that the lineal-path function (orange curve) exhibits higher values than other SMDs, except for S_2. This indicates that linear propagation is the dominant pattern in the evolution of the pores, which is evident from the snapshots. In both the XY and the XZ planes, S_2 shows higher values than the other SMDs. This is because it is more likely for two random points to be in the same phase of interest than for multiple points.

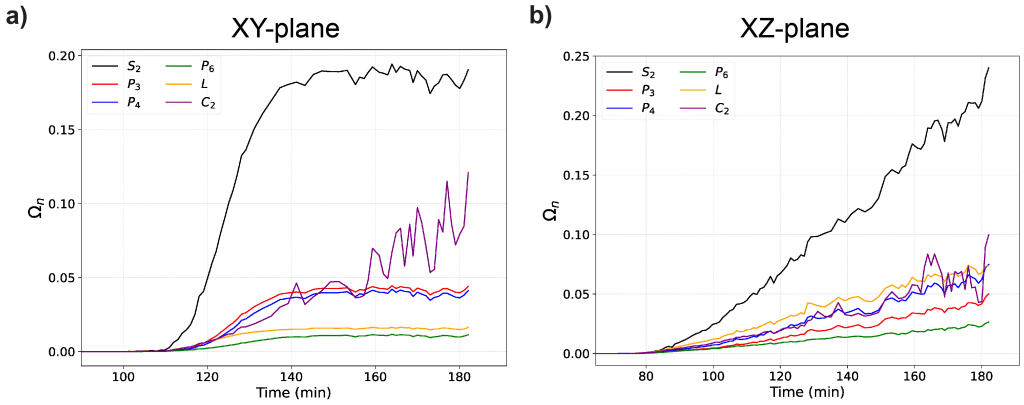

Figure 5. Quantification of the dynamics of the generated pore networks in Exp 1. (a) Evolution of SMDs calculated using Ω_n metric over time in the XY plane (b) Evolution of pore space in the XZ plane. Examples of snapshots in both planes at different time steps are presented in Figure 4.

In Exp 2, we performed a similar analysis on orthogonal slices of 3D volumes cropped from the bottom of the sample shown in the leftmost image in Figure 2b. Figure 6a presents the original greyscale snapshots, highlighting the ROI with a red box for the XY plane and a green line for the XZ plane. The segmented images across these planes are shown in Figures 6b and 6c, respectively. It should be mentioned that the sample jacket in the cell collapsed in the lower part of the sample once the reaction interface reached the outer surface of the sample after approximately 75 minutes, as shown in Figure 6a. This caused a slight movement in the lower part of the sample around the drilled hole. To correct for this misalignment, the greyscale images were registered by applying a rigid transformation (i.e., translation and rotation) using the pystackreg python library (Thevenaz et al., 1998).

Figure 7 presents the metrics Ω_n versus time in Exp 2 in the XY and XZ planes. In Figure 7a, it can be seen that the lineal path function (L) exhibits higher values than the higher-order polytope functions (e.g., P_3 and P_4) up to approximately 100 minutes, meaning that the linear patterns (i.e., channels observed in the XY plane (Figure 6b)) propagate faster than other geometric patterns. After 100 minutes, this linear evolution slows down and reaches a plateau. A reduction in the rate of evolution is also observed in other SMDs between 100 and 120 minutes. After 120 minutes, a faster increase in P_3 and P_4 compared to L suggests a complex spatial evolution of the reaction-induced pore network. However, in the XZ plane, P_3 and P_4 evolve more rapidly than linear connectivity, consistent with observations in the XZ plane, as shown in Figure 6c. In both planes, cluster connectivity (c_2) shows higher values, more fluctuations, and evolves faster than other SMDs, except for S_2, as discussed earlier.

In addition to the 2D analysis, we quantified the evolution of microstructures by calculating S_2 and its scaled version F_2, using 3D images over time. F_2 function, also known as the autoscaled covariance function, normalises S_2 by the phase fraction (i.e., porosity), allowing us to capture the evolution of the structural features of the pore space, independent of porosity. This makes F_2 particularly useful for comparing microstructures with different porosities (Amiri, Vogel, & Plümper, 2024).

Figures 8a and 8b present the 3D evolution of the reactive pore network in Exp 1 and Exp 2, respectively. In Exp 1, Ω_{S_2} increases almost linearly with some fluctuations over time, while Ω_{F_2} shows a sharp increase at early times, peaking around 100 minutes. After this period, Ω_{F_2} begins to decline and stabilises around 150 minutes. For Exp 2, as shown

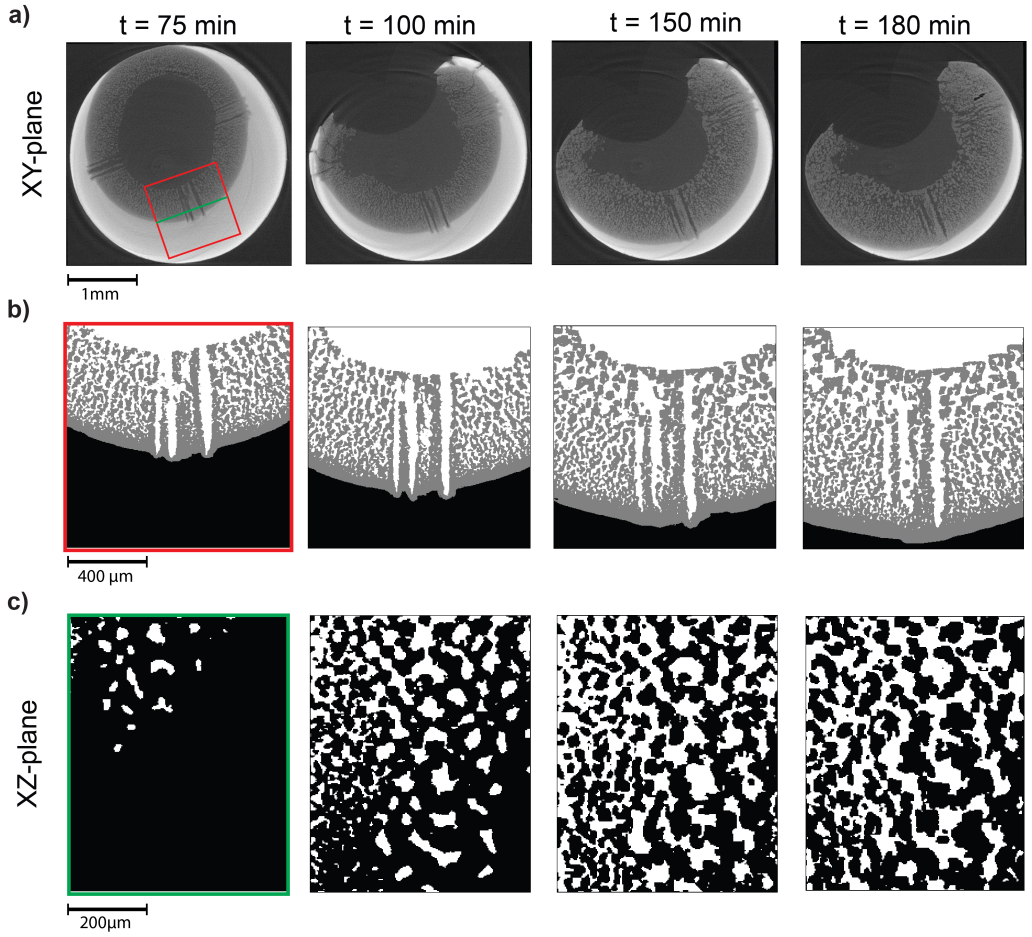

Figure 6. Snapshots of 3D volume slices at different planes and times in Exp 2. (a) Original greyscale images in the XY-plane, with the red box and green line indicating the locations of the XY- and XZ-planes, respectively. b) Segmented images corresponding to the region highlighted by the red box in (a). Here white, grey, and black pixels represent pores, reacted zone (i.e., replaced K(Br, Cl)), and unreacted KBr crystal, respectively. (c) Binary segmented images across the XZ-plane, where white pixels indicate pores and black pixels represent other phases.

in Figure 8b, Ω_{S_2} exhibits a slow increase of up to approximately 80 minutes, followed by a more rapid evolution of up to approximately 100 minutes. After this point, it continued to increase at a slower rate until the end of the experiment, with a sharp drop in the final minutes. Here, Ω_{F_2} indicates rapid microstructural evolution early on, peaks around 80 minutes when it stabilises transiently. Following this period, the curve starts to decline, indicating that the rate of changes slows down towards stability. A notable feature in both experiments is the large fluctuations in all curves throughout the experiments. This can be seen in $\delta\Omega_{F_2}$ (green curve), which measures the difference in F_2 between two consecutive images. Specifically, the $\delta\Omega_{F_2}$ curves in both experiments show high fluctuations around zero, with more positive values at initial times and more negative values when Ω_{F_2} starts declining, eventually hovering close to zero at the end of the experiments.

Figure 9 presents the average chord length, $\bar{l_c}$, calculated using Equations 2 and S_2 derived from 3D binary images over time. In Exp 1, $\bar{l_c}$ rises sharply from 70 to 90 minutes, followed by a slow gradual increase from 30 to 35 μm over the next 90 minutes until the end

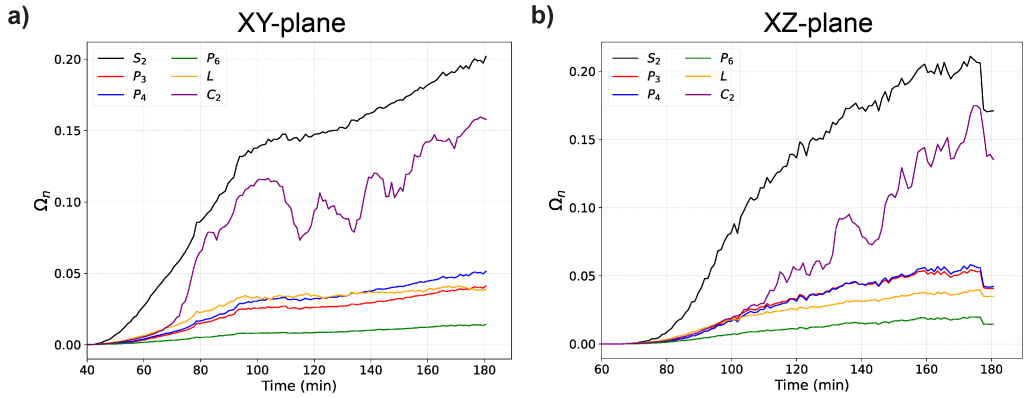

Figure 7. Quantification of pore network evolution using the Ω_n metrics in Exp 2. (a) Evolution of SMDs in the XY plane. The reaction reaches the selected slice in the middle of the 3D volume (Figure 2b) after 40 minutes, leading to the development of patterns in this slice thereafter. (b) Evolution of SMDs in the XZ plane in the selected slice shown in Figure 6c.

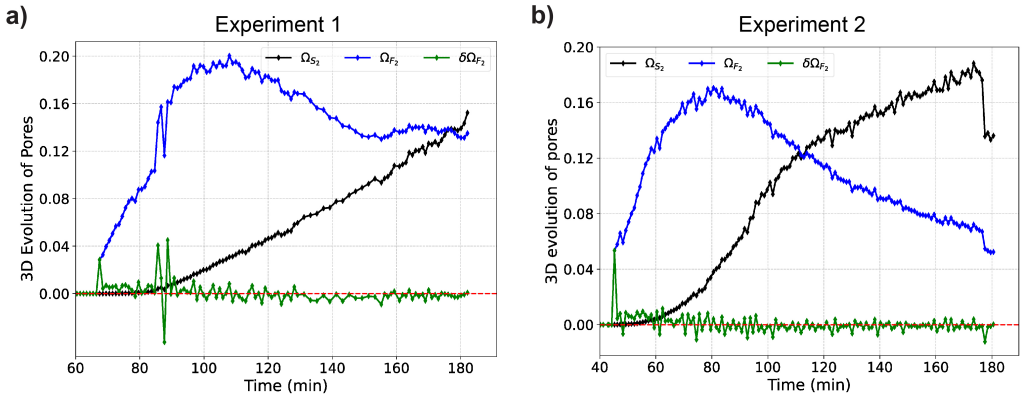

Figure 8. The evolution of pore space in 3D volumes from both experiments. (a) Evolution of porosity in 3D using S_2, F_2, and $\delta\Omega_{F_2}$ in Exp 1. The latter shows the changes in the pore structures compared the previous 3D volume. (b) Changes in 3D pore space over time in Exp 2. The F_2 correlation highlights the evolution of pores in terms of their structural properties, independent of changes in porosity.

of the experiment. In Exp 2, as shown in Figure 9b, $\bar{l_c}$ exhibits a marked increase from 45 to 80 minutes, then decreases slightly to about 120 minutes, despite a local anomaly before 100 minutes. After 120 minutes, a gradual increase in $\bar{l_c}$ is observed.

3.2 Reaction front velocity

The location of the reaction interface can be determined from the segmented images, specifically from the interface between the grey and black phases, as shown in Figures 4b and 6b. Figures 10a and 10b show the interface displacement over time in Exp 1 and Exp 2, respectively. The interface locations are depicted at fixed time intervals of 20 minutes in Exp 1 and 40 minutes in Exp 2. These figures reveal that, unlike Exp 1, which shows no significant change, the reaction front in Exp 2 moves rapidly at the beginning. Then it

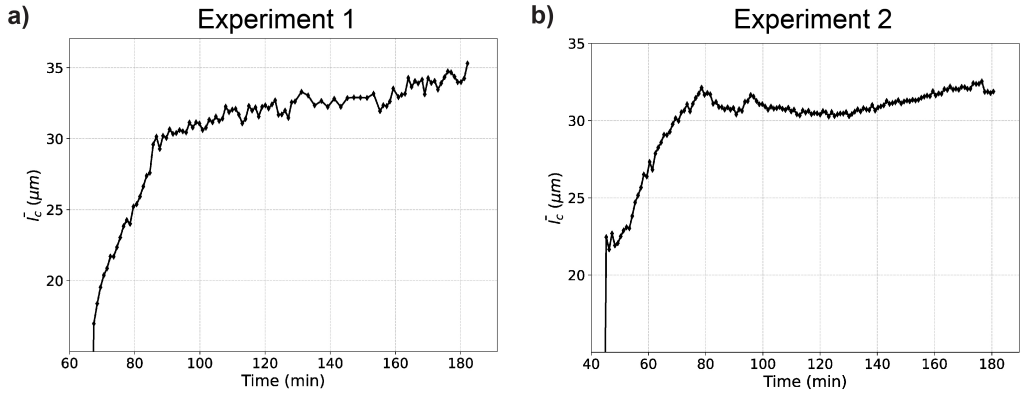

Figure 9. Average chord length ($\bar{l_c}$) calculated from S_2 in 3D. (a) Evolution of $\bar{l_c}$ over time in Exp 1, showing a sharp initial increase until 90 minutes, followed by a slower rise thereafter. (b) Variations of $\bar{l_c}$ over time in Exp 2.

slows down with time, as evidenced by the decreasing distances between the curves. These locations were then mapped on a regular Cartesian grid based on the pixel size (2.75 μm), and the local reaction rate was calculated using (Noiriel et al., 2020):

$$V_r = \frac{dI_r \cdot n}{dt} \tag{8}$$

where I_r and dI_r represent the position vector of the reaction interface and the displacement of the interface, respectively, n is the normal vector of the interface and dt is the time interval.

Figures 10c and 10d show the velocity profiles along the interfaces in both experiments. These figures reveal highly heterogeneous velocity profiles early on in both experiments, with higher localised velocities in front of the channels (that is, valleys in Figures 10a and 10b). In Exp 2, the velocity is also significantly higher at the edges, up to approximately 90-100 minutes. After this period, the propagation of the channels slows significantly and eventually ceases in the last minutes, resulting in a smoother and flatter interface. A similar trend of interface smoothing and velocity reduction can be observed in Exp 1, albeit to a lesser degree.

To estimate the overall reaction velocity, we averaged the velocity values at different positions on the interface at each time. Figure 11a shows that in Exp 1, the reaction rate is around 3 $\mu m/min$ at the beginning and gradually decreases with oscillations. In Exp 2, the reaction front proceeds rapidly early on (about 7 $\mu m/min$), followed by a quick reduction by 57 percent to around 3 $\mu m/min$ until about 80 minutes. After this point, despite the high fluctuations, the average velocity does not show a significant reduction until approximately 100 minutes. This stage is followed by another marked drop in the velocity, slowing to around 1 $\mu m/min$ and stabilising after 120 minutes.

3.3 Evolution of Minkowski functionals

Figure 12 presents the changes in the three MFs calculated from binary 3D images at different times. From Figures 12a and 12b, it can be seen that the specific surface area (S_v) of the pore space in both experiments increases over time, following a trend similar to that obtained from Ω_{S_2} (that is, black curves in Figure 8). The specific integral mean curvature (M_v) of the reaction-induced pore space shows a rapid increase during the early phase of both experiments. This fast evolution then slows down in Exp 1, stabilising after 140 minutes

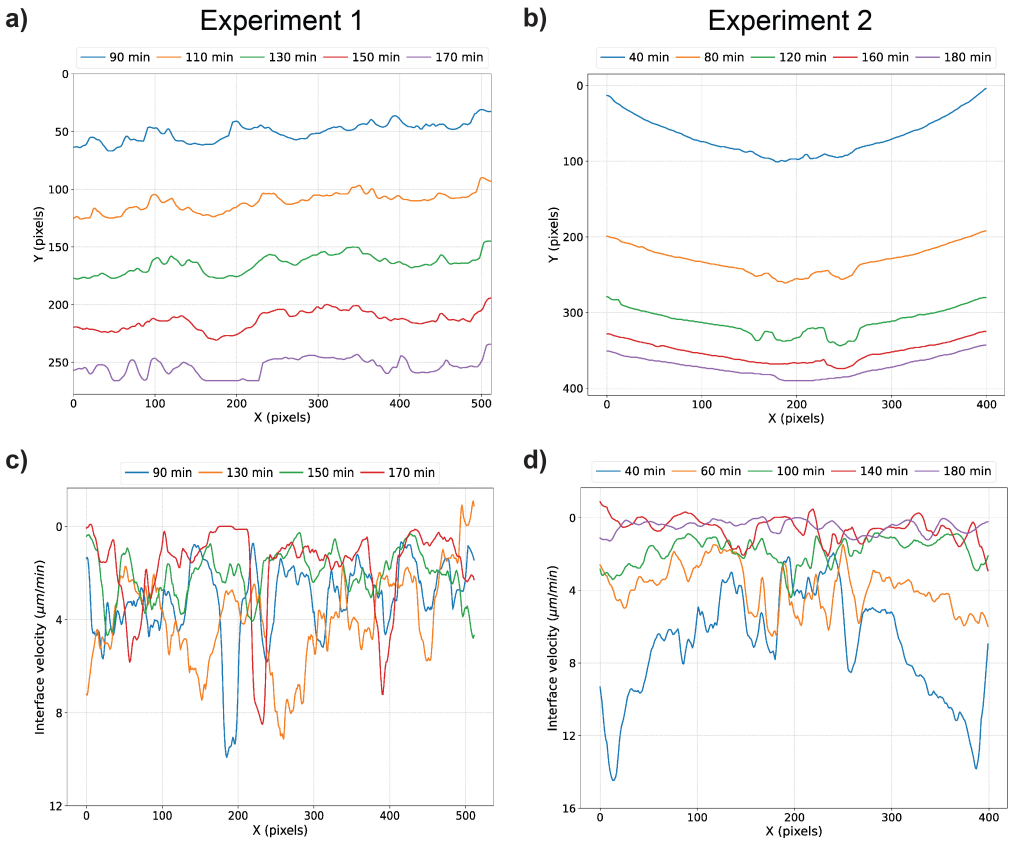

Figure 10. Locations of reaction fronts and velocity profiles at different time steps.(a) and (b) present the reaction front locations in Exp 1 and Exp 2, respectively. (c) and (d) show the velocity profiles, calculated using Equation 8, for these experiments.

(Figure 12c). For Exp2, M_v decreases after peaking and transiently stabilising between 110 and 130 minutes (Figure 12d). Evaluation of the specific Euler characteristic (χ_v), as shown in Figure 12e-f, indicates that the reaction-induced pore space is not connected at the beginning, as expressed by hovering close to zero. However, a decrease in χ_v towards negative values shows that the pore networks become highly connected in both experiments. Here again, a steady state can be observed in the late phase when the connectivity remains largely unchanged, despite the observed fluctuations.

3.4 Evolution of transport properties

As discussed above, ICDP mechanisms generate transient porosity during KBr-KCl replacement. The reaction-induced pore space and its characteristics (e.g., pore size and pore connectivity) change with time in a complex manner, leading to the evolution of the flow and transport properties of the system, such as permeability. It is worth mentioning that the total permeability across the whole sample is nearly zero as the pores are dead-end, and the permeability we refer to here is the local permeability estimated at the ROIs assuming periodic boundary conditions.

To estimate permeability, we use a voxel-based finite element method (FEM), as detailed in (Lopes et al., 2022, 2023). Periodic boundary conditions, low Reynolds number (no turbulent flow), and no significant change in velocity are the underlying assumptions used

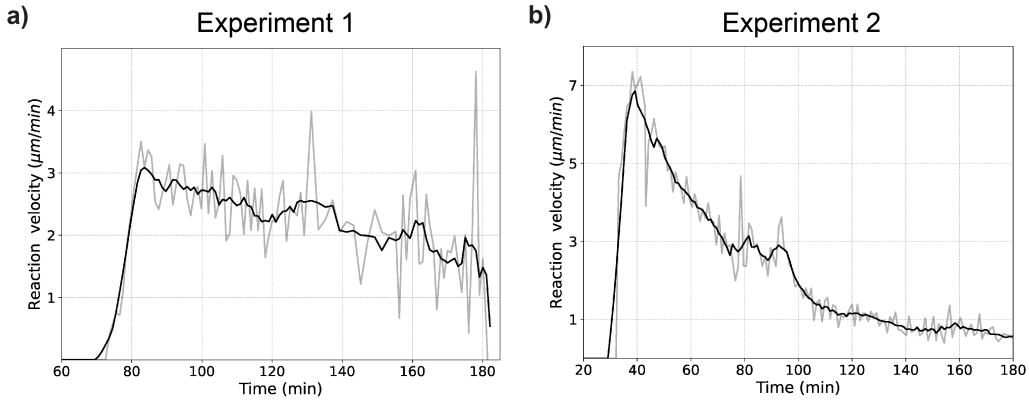

Figure 11. Average reaction velocity over time in both experiments. (a) Changes in the average reaction velocity in Exp 1, calculated by averaging the velocity along the reaction front at different times, as shown in Figure 10c. (b) Average reaction velocity over time in Exp 2. The lighter shaded curves indicate the average velocity, showing significant oscillations, especially in Exp 1. The darker black curves represent the moving average computed from these shaded curves to highlight the overall trends.

in this method, reducing the Navier-Stokes equations to Stokes flow. In addition to the validity of these assumptions in our case, this method is particularly suited to our study for two reasons. Firstly, it requires only a binary 3D image as input for the simulation. Secondly, it can be implemented on a GPU, which is crucial considering the large number of 3D images in our study.

Figure 13 shows the time-resolved variations in porosity (black curve) and directional permeabilities (coloured curves) for both experiments, with the blue curve representing the average permeability on three axes. In Exp 1, it can be seen that a few percent increased porosity at the beginning of the reaction (from 70 to 90 minutes) results in an abrupt increase in permeability across all directions. After 90 minutes, although the induced porosity increases almost linearly until the end of the experiment, the permeability increases at a slower rate and begins to diverge along different directions until 150 minutes. After this period, the rate of increase in permeability slows down further and stabilises. Similarly, an initial rapid increase in permeability is observed in Exp 2 from 45 to 80 minutes when porosity increases slowly, as shown in Figure 13b. Between 80 and 100 minutes, we can see rapid pore generation, increasing the total porosity from 0.1 to 0.25, and an anisotropic rise in permeability across different directions. This period is followed by a turning point in the porosity curve at 100 minutes when the rate of porosity generation slows down while the directional permeabilities start to converge. The last few minutes of this experiment are marked by a sharp drop in both porosity and permeability.

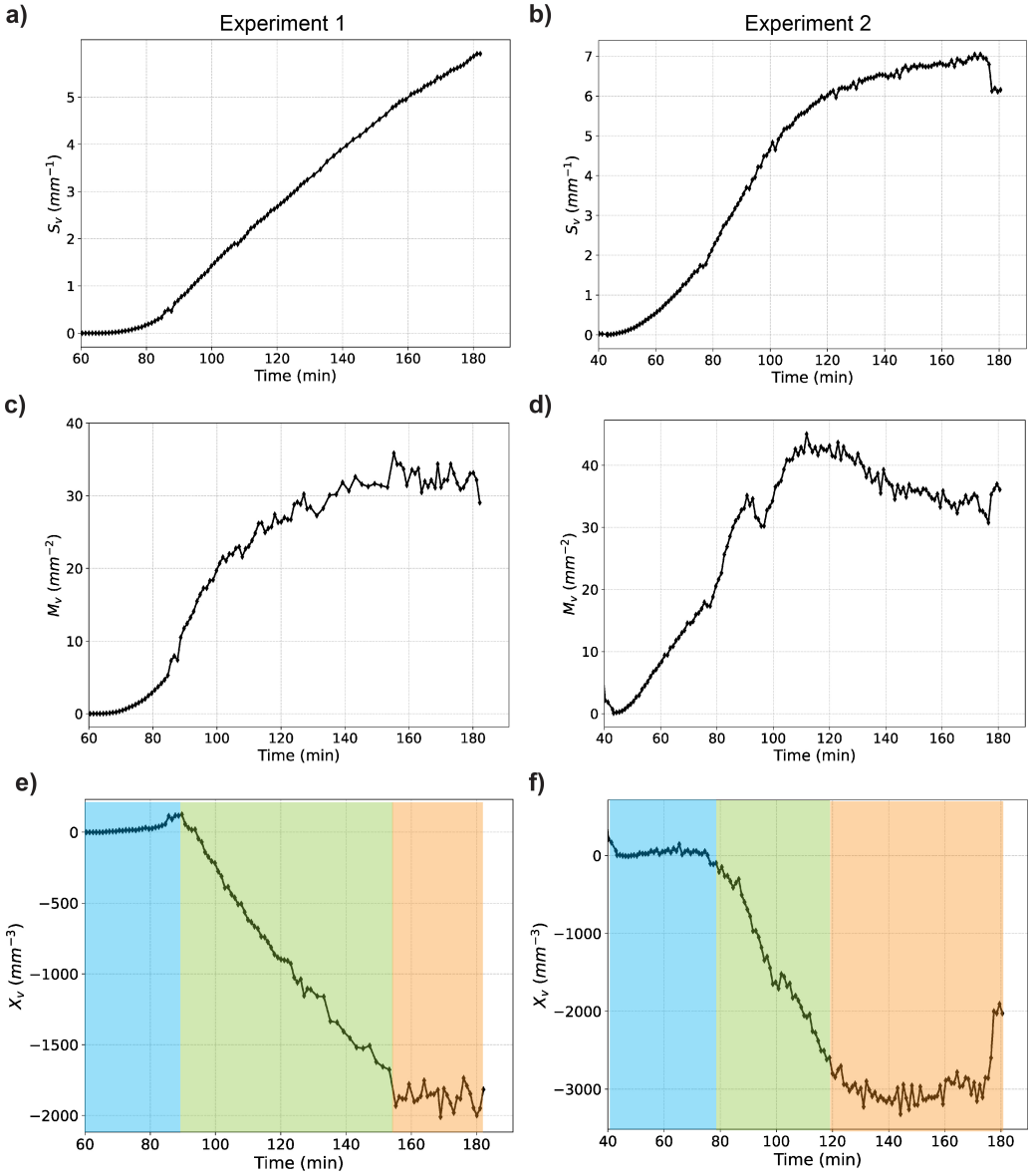

Figure 12. Minkowski functionals of pore space in both experiments. (a) and (b) show the specific surface area, S_v, in Exp 1 and Exp 2, respectively. (c) and (d) present the results of the specific integral mean curvature, M_v, in Exp 1 and Exp 2. (e) and (f) depict the specific Euler characteristic, χ_v, in Exp 1 and Exp 2. Note that the more negative the χ_v, the more connected the pore network. Colours in Euler connectivity plots highlight different stages during the microstructure evolution (discussed in the next sections).

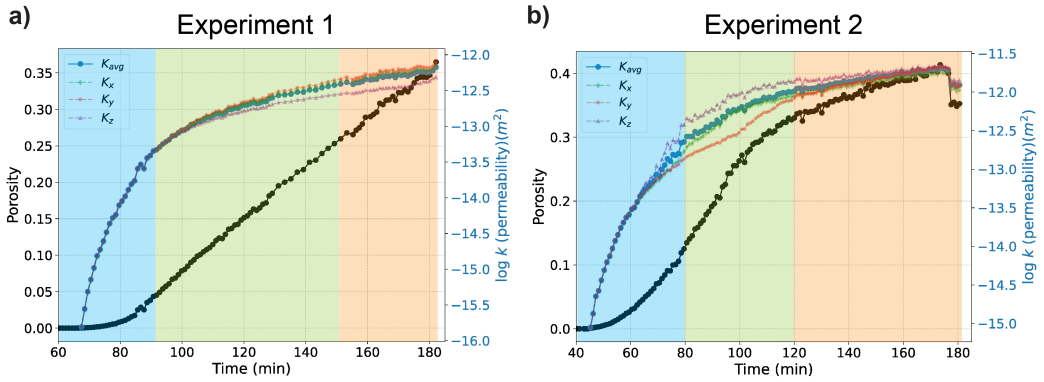

Figure 13. Evolution of porosity and local permeability during KBr-KCl replacement. The graphs depict the changes in porosity (black circles) and permeability (coloured symbols) over time for two experiments. (a) Exp 1 shows the gradual increase in porosity and permeability, with the permeability represented by average permeability (K_{avg}) and directional permeabilities (K_x, K_y, K_z). (b) Exp 2 illustrates a similar trend of average permeability but with distinct differences in the evolution of porosity and directional permeabilities. Colours indicate different stages of porosity and permeability evolution (see the following section for more details).

3.5 Correlation analysis

Our results reveal that reaction-induced pores undergo complex changes in structural and morphological properties. These properties exhibit distinct trends during different stages of the replacement reaction. Specifically, three stages may be distinguished in both experiments: an initial stage of rapid evolution, a transition stage, and a steady-state stage.

We calculated the Pearson correlation coefficient (PCC) for each stage to elucidate the interrelationships between the quantified parameters. The PCC is a statistical measure of the linear association between two variables, with values ranging from -1 to 1. A positive PCC indicates a positive correlation, a zero value signifies no correlation, and a negative PCC indicates an inverse correlation between the two parameters (Pearson, 1896; Rodgers & Nicewander, 1988). Figure 14 presents the correlation matrices between the average permeability, porosity (ϕ), $\bar{l_c}$, and MFs in the three stages. To facilitate interpretations, we computed the PCC of -χ_v with other variables, as its negative values mean more connectivity. Stage 1, characterised by rapid evolution, spans 70 to 90 minutes in Exp 1 and 45 to 80 minutes in Exp 2. Stage 2 extends from 90 to 150 minutes in Exp 1 and 80 to 120 minutes in Exp 2. Stage 3 is defined as 150 to 180 minutes in Exp 1 and 120 to 180 minutes in Exp 2.

The results of the correlation analysis show that the average permeability, porosity and specific surface area (S_v) are strongly correlated in both experiments at all stages. In stage 1, Figures 14a and 14d show the correlation matrices in Exp 1 and Exp 2, respectively. The results indicate a strong positive dependency between permeability and other parameters except for -χ_v, whose correlation coefficient with permeability is -0.85 in Exp 1 and 0.16 in Exp 2. During stage 2, we find a strong relationship between all properties of the pore space in Exp 1 (Figure 14b). However, there is a negative correlation between $\bar{l_c}$ and other variables in Exp 2, as shown in Figure 14e. The interrelationships between variables are more complex in stage 3. As can be seen in Figures 14c and 14f, there is almost no correlation between permeability and connectivity (-χ_v). In addition, it can be seen that the integral mean curvature (M_v) is negatively correlated with other parameters, especially

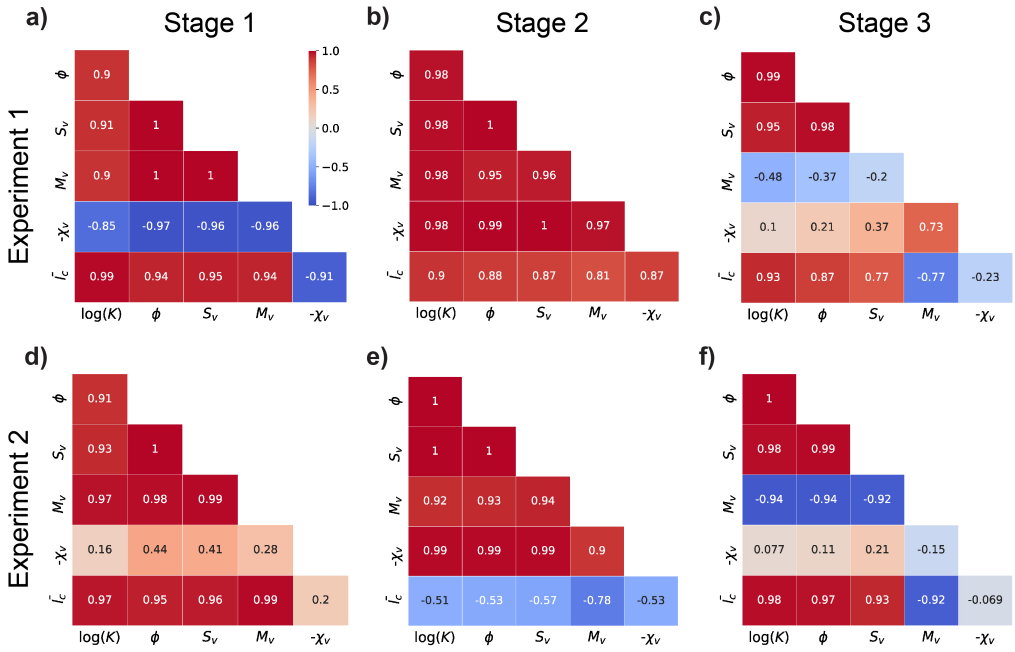

Figure 14. Correlation analysis of various parameters across different reaction stages. (a)-(c) show the correlation matrices for different parameters during the three stages in Exp 1. (d)-(f) present the correlation matrices for different parameters during the three stages in Exp 2.

the large negative values found in Exp 2 (Figure 14f). The interpretation of these evolving correlations, together with the results of other analyses, and their implications for porosity evolution and pore-scale processes during the different reaction stages, are discussed in detail in Sections 4.1–4.3 and 4.5.

4 Discussions

Fluid-mediated mineral replacement often produces transient, interconnected pore networks that facilitate reaction progression (Beaudoin et al., 2018; Kar et al., 2016; C. V. Putnis & Mezger, 2004; Raufaste et al., 2011). In this study, operando time-resolved synchrotron tomography was used to track pore space evolution during KBr–KCl replacement. Quantitative analyses using spatial correlation functions and morphological measures revealed three distinct stages of structural change and their associated effects on transient permeability. These stages are described in detail below.

4.1 Stage 1: Rapid Evolution

The first stage, approximately 70 to 90 minutes for Exp 1 and 45 to 80 minutes for Exp 2, is characterised by a rapid evolution of reaction-induced pores, evidenced by a sharp increase in Ω_{F_2} in 3D (Figure 8). During this stage, a heterogeneous velocity is observed along the rough reaction interface (Figure 10) and a relatively high reaction rate is found (Figure 11). We attribute rapid replacement to the development of pore channels (Figures 4b and 6b) along the main crystallographic axes of the cubic KBr crystal, providing effective pathways for fluid access to the reaction interface. Consequently, the reaction progresses faster in front of these channels, which remain disconnected during this stage (Figures 4 and 6c), resulting in a rough interface and high variations along the interface.

During this stage, despite a slight increase in porosity, local permeability exhibits an increase of several orders of magnitude in all directions, as shown in Figure 13. This significant increase in permeability is likely due to the generation and widening of channels rather than an enhancement in the connectivity of the pore network. Rapid growth in the size and elongation of the generated channels is demonstrated by the sharp increase in $\bar{l_c}$ (Figure 9). Furthermore, Figures 12e and 12f indicate that the pore network remains largely disconnected during this stage, as reflected in the positive values in Exp 1 and the small negative values in Exp 2. The results of correlation analysis (Figures 14a and 14d) show the highest positive correlation coefficient between permeability and $\bar{l_c}$. In contrast, the coefficient between permeability and connectivity (-χ_v) is negative in Exp 1 and slightly positive in Exp 2.

The rough reaction interface (Figure 10) and relatively rapid replacement (Figure 11) observed during the initial minutes of KBr-KCl replacement have also been reported by previous studies (Beaudoin et al., 2018; Kar et al., 2016; Raufaste et al., 2011). These studies attributed these observations to an advection-driven transport regime through channelised pores. Koehn et al. (2021) demonstrated that rough reaction fronts develop predominantly when advection is the main transport process (i.e., high Péclet number) and the reaction rate is slow, ranging from 10^{-8} to 10^{-7} m/s, which is consistent with our findings. Consequently, we conclude that advection is the dominant transport regime during this stage. An additional transport mechanism in these dead-end pores could be the self-generated convective flow driven by diffusion-osmosis. In this process, an ion gradient (e.g., between K^+, Br^-, and Cl^-) acts as an electric pump, facilitating ion circulation within the dead-end channels. This mechanism sustains the reaction and allows channel propagation (Ajdari & Bocquet, 2006; Kar et al., 2015, 2016; Plümper et al., 2017a).

4.2 Stage 2: Transition

The second stage can be defined as occurring between 90 and 150 minutes for Exp 1 and between 80 and 120 minutes for Exp 2. This stage is marked by a change in the behaviour of Ω_{F_2}, which initially fluctuates around its maximum values before starting to decrease. Furthermore, the average chord length ($\bar{l_c}$) evolves much more slowly during this stage than in stage 1 (Figure 9). These features signify a transition period from the initial rapid evolution towards a steady state.

During this transition stage, the connectivity of the reaction-induced pore networks is significantly enhanced, evidenced by a sharp decrease in the specific Euler number, χ_v, towards negative values (Figures 12e and 12f). Our correlation analysis, presented in Figures 14b and 14e, reveals high correlation coefficients between average permeability and χ_v, indicating that the connectivity of the pores is a major contributing factor to increased permeability. However, despite the sharp increase in connectivity and a faster increase in porosity (Figure 13) during this period, the results indicate a slower evolution of permeability in both experiments (Figure 13). This slower increase in permeability can be explained by the increase in the integral mean curvature (Figures 12c and 12d), which corresponds to a more tortuous pore space. In contrast to stage 1, the significant positive correlation coefficients found between χ_v, S_v and porosity suggest that new pores are generated along the walls of the channels rather than their tips, creating lateral connections between channels. The enhancement of connectivity is also evident in Figures 5 and 7, which show an increase in the cluster connectivity of pores in the 2D planes for Exp 1 and Exp 2, respectively.

Figure 11 shows that while the reaction velocity in Exp 1 decreases gradually with significant fluctuations, Exp 2 exhibits a sharp drop around 100 minutes. This point corresponds to a transient drop in porosity (Figure 13b) and a rise in χ_v (Figure 12f), indicating a minor increase in precipitation. However, it is the location of the precipitates, rather than their amount, that causes the sharp drop in reaction velocity. Close inspection

of the snapshots at 75 and 100 minutes in Figure 6b reveals that precipitation occurs mainly at the inner rim of the crystal, thus limiting fluid flow to the channels. This partial inlet clogging also slows the convection cell driven by diffusion-osmosis within the channels, although this mode of transport has not been explicitly taken into account here. Furthermore, as the channels propagate, advection becomes less effective with increasing distance from the KCl source. These factors likely contribute to slower channel propagation and increased lateral connectivity, causing the directional permeabilities to converge after 100 minutes. Consequently, this leads to a more homogeneous velocity profile, a smoother reaction front (Figure 10), and a reduced average reaction velocity (Figure 11). Specifically, the reaction front in Exp 2 evolves from a curved to a flatter shape. Overall, the transition towards more uniform permeability, a smoother front, and a homogeneous velocity profile at slow reaction velocity indicate a reduction in Péclet number (Koehn et al., 2021), signifying a change from an advective to a diffusion-driven transport regime in Exp 2.

4.3 Stage 3: Steady state

The final stage of mineral replacement begins at 150 minutes for Exp 1 and 120 minutes for Exp 2 until the end of the experiments. During this stage, the generated pore space stabilises with respect to its structural and morphological properties. In Exp 1, Ω_{F_2} reaches a plateau following the decline observed in the transition stage, and $\delta\Omega_{F_2}$ shows smaller fluctuations, converging toward zero, which indicates minimal changes in the pore structures (Figure 8a). This stabilisation is also evident in M_v and χ_v, as depicted in Figures 12c and 12e, respectively. A similar trend is observed in Exp 2, except that Ω_{F_2} continues to slowly decrease, exhibiting several transient steady states.

Figure 13 illustrates that, despite the increase in porosity, the evolution of the permeability slows down and eventually stabilises during this stage. However, stabilisation of χ_v at large negative values indicates that the reaction-induced pores remain highly connected without significant changes during this stage. Consequently, the small increase in permeability is probably not related to connectivity, as supported by the small correlation coefficients between the average permeability and χ_v in both experiments (Figures 14c and 14f). The correlation matrices reveal a strong correlation between permeability and $\bar{l_c}$ in both experiments, consistent with the slow increase in $\bar{l_c}$ (Figure 9). This gradual increase in $\bar{l_c}$ could be attributed to the coarsening of the pores and the decreased tortuosity. The latter is particularly likely in Exp 2, where a decrease in M_v is observed (Figure 12d), and there is a large negative correlation between M_v and other variables. Therefore, the slight increase in permeability during this stage could be explained by pore coarsening and a reduction in the curvature of the pore space, resulting in less tortuosity.

Moreover, in Exp 2, the steady-state stage is characterised by the convergence of directional permeabilities, further smoothing of the rough reaction front (Figure 10b), reduced velocity variations along the interface (Figure 10d) and a steady slow reaction velocity (Figure 11b). These observations indicate that diffusion is the dominant mode of transport, consistent with previous studies (Beaudoin et al., 2018; Koehn et al., 2021; Raufaste et al., 2011; Steefel et al., 2015; Szymczak & Ladd, 2014). However, Figure 11 shows that the reaction velocity decreases more slowly with sharp oscillations in Exp 1 compared to Exp 2. Furthermore, the reaction front in Exp 1 remains relatively rough (Figure 10a), and the velocity profiles show more variations (Figure 10c). In contrast to Exp 2, permeability along different axes continues to diverge in Exp 1.

4.4 Exp. 1 vs. Exp. 2

Although we observed a similar evolution of pores in both experiments in terms of different structural and morphological properties, a few differences between the two experiments can be noticed. First, in contrast to Exp 2, the reaction interface remains more or less rough in Exp 1 during the three stages (Figure 10a). Furthermore, comparing Figures 10c and

10d, the velocity along the reaction front is not as homogeneous as that observed in Exp 2, evidenced by the spikes in the velocity profiles at 150 and 170 minutes in Figure 10c. The sustained roughness of the reaction front in Exp 1 can be attributed to the more channels generated compared to Exp 2, as shown in Figures 4b and 6b, as well as supplementary videos S1 and S2 for Exp 1 and Exp 2, respectively. These channels, which are also wider in Exp 1, provide straight and effective pathways for species transport to the reaction interface ahead of the channels, leading to an unstable and heterogeneous velocity profile (Figure 10c). The development of a rough and unstable reaction front can be related to a high Péclet number (Koehn et al., 2021; Min et al., 2016), indicating that advection is likely the dominant transport regime in Exp 1. Furthermore, unlike Exp 2, there is no evidence for channel clogging due to precipitation of K(Br, Cl) near the inlet in Exp 1. Instead, it appears that precipitation occurs more uniformly along the channels, creating dendrite-like patterns. This is consistent with the findings of Tartakovsky et al. (2007), which show that pore clogging near the inlet occurs in the case of low Péclet number (i.e., diffusive transport), while uniform precipitations are observed along the main flow paths when advection is the most dominant mode of transport. The advection transport along the channels hinders the lateral connection of the channels and may explain the lower connectivity of the generated pores, as indicated by the smaller negative value of χ_v in Exp 1 (about -2000 mm^{-3}) compared to Exp 2 (about -3000 mm^{-3}), as shown in Figures 12e and 12f. The lower connectivity can, in turn, explain the anisotropic flow in Exp 1 (Figure 13a), while the highly connected pore network resulting from diffusive transport in Exp 2 leads to uniform permeability along axes (Figure 13b).

These discrepancies may be linked to the difference in the experimental configuration of experiments, specifically Exp 2 is performed in the pressurised cell with a curvy initial interface between KCl fluid and KBr crystal. In Exp 1, KCl drops are supplied onto the top of a cubic KBr crystal with an initially flat interface, providing fresh KCl fluid to the system. The fresh fluid, combined with the flat interface and the force of gravity, may contribute to the formation of more channels. In contrast, injecting the KCl fluid from the central hole in Exp 2 exerts a radial pore pressure on the inner circular rim of the crystal in different orientations. This can cause competition between channels in different directions, leading to the creation of more wormhole patterns and fewer channels.

Our results also show that there is a sharp drop in different parameters, including porosity and permeability (Figure 13b), Ω_{S_2}, and Ω_{F_2} (Figure 8b) in the last minutes of Exp 2. These observations, along with a marked increase in χ_v (indicating a decrease in the connectivity of the pore network), indicate a rapid precipitation, as shown in the snapshots in Figure 6b. As discussed earlier, precipitation at the inner rim appears to begin during the transition stage; however, it accelerates significantly in the last few minutes of the steady-state stage, leading to nearly complete blockage of fluid access to the reaction interface. The observed pore closure at the rim could be explained by the fluid becoming critically supersaturated, leading to rapid overgrowth of K(Br, Cl).

4.5 Porosity evolution

Our findings show a complex and highly dynamic porosity evolution through different stages during KBr-KCl replacement. Similarly to previous work (Beaudoin et al., 2018; Kar et al., 2016; Raufaste et al., 2011), we observed channel-shaped porosity developing during the rapid evolution stage. Raufaste et al. (2011) observed disc-shaped cavities perpendicular to the channels and small pores connecting the tip of the channels to the reaction front. In our study, although we can see these small pores in the greyscale images, we could not segment them because of the limited resolution. However, the disc-shaped cavities, which appear dendrite-shaped, can be observed in 2D snapshots in Figures 4b and 6b.

Although the channels maintain their overall structure and position, they begin to coarsen during the transition stage, as shown in Figures 4a and 6c. This observation is

consistent with previous research (Beaudoin et al., 2018; Raufaste et al., 2011). Beaudoin et al. (2018) attributed this coarsening to a higher chemical gradient in the channel walls than along the channel length, particularly when the channels elongate. This leads to the creation of pores on the walls of the channels rather than their tips. As discussed earlier, this also results in a significant increase in the pore connectivity, especially in Exp 2, where precipitation blocks the fluid inlet, causing diffusion to become the dominant transport mechanism.

An additional finding is that, while porosity structures do not show significant changes during the steady state, it appears that pores transition into more tabular forms with straight edges, as seen in Figure 4a for Exp 1 and Figure 6 for Exp 2. Specifically, this is more pronounced around the inner rim, where the precipitation occurred mainly in Exp 2. This change in porosity morphology is also confirmed by a decrease in the integral mean curvature, (M_v), indicating more straight pores, especially in Exp 2 (Figure 12d), where significant negative correlation coefficients are also found between M_v and other variables (Figure 14f). The evolution of SMDs in 2D planes further demonstrated a more regular pore shape, as indicated by the larger Ω_n for the triangular (P_3) and square (P_4) patterns compared to the lineal path (L) in Figures 5a and 7. This transition into more regular patterns can be explained by the epitaxial growth of KCl on the cubic parent KBr crystal. At the start of the dissolution-precipitation process, pores form in irregular, curvy shapes because of nonuniform initial dissolution rates and local variations in supersaturation. However, as the reaction progresses, the epitaxial growth of KCl on the KBr crystal surface becomes predominant. During this growth, KCl adopts the cubic crystal structure of KBr, resulting in the crystallographic orientations of the newly formed KCl aligning with those of the underlying KBr.

Beyond these aspects of porosity evolution at different stages, additional observations add to the complexity of quantifying reaction-induced pore space development. The analyses reveal substantial fluctuations in various properties of the reaction-induced porosity, even during the steady-state stage. This suggests that the porosity generated during the KBr-KCl replacement is highly dynamic. These fluctuations indicate a re-equilibration process, resulting from complex interactions between dissolution and precipitation processes that continuously modify the pore space. The supplementary videos S1 and S2 illustrate that while the overall structure of the generated channels remains stable, these fluctuations stem from the ongoing evolution of smaller features.

Our findings show that dissolution and precipitation processes cause substantial changes in the pore structures and morphology. Our quantification of reaction-induced porosity indicates that a same increase in total porosity can have different impacts not only on transport properties (e.g., connectivity and permeability) but also on their interdependencies in space and time as the pore structure and morphology is modified. Specifically, our results suggest that the feedback relationships between pore space characteristics and transport properties depend on complex interactions between transport regime and dissolution and precipitation processes. Our study shows that the amount and, more importantly, the distribution of the precipitates can have a crucial impact on the evolution of pore structures. For instance, as illustrated in Exp 2, small amounts of precipitates near the inlet may clog the channels, which in turn results in the transition toward diffusive transport, increased connectivity of the pore space, and changes in flow pattern from the channels towards low-permeable zones. This phenomenon, which can be described as 'dechannelising', can eventually lead to a more uniform transport pattern.

These complexities, along with the dynamic nature of the reaction-induced porosity, make the parameterisation of these evolving systems challenging for reactive transport modelling, which has many applications in natural environments and geo-engineering problems. Numerous studies have investigated the relationships between porosity and other transport parameters, such as tortuosity (Ray et al., 2018; Xie et al., 2015), permeability (Hommel et al., 2018; Poonoosamy et al., 2021), and reaction rate, often linked to surface

area (Andreani et al., 2009; Luhmann et al., 2014). However, these relationships usually involve at least one empirical fitting parameter derived under certain circumstances in a specific system. Moreover, this fitting parameter itself has been shown to evolve depending on the dominant transport regime, as well as the dissolution and precipitation patterns (Menke et al., 2016; Smith et al., 2013), thus limiting the predictive capabilities of these relationships. Therefore, it seems unlikely that a single model could accurately describe the complex feedback interrelationships between different parameters in such highly dynamic systems. Our study suggests that an integrated and adaptive approach, which links the transport properties to the structural and morphological characteristics of the pores, may offer a more effective solution.

5 Conclusions

We investigated the evolution of reaction-induced porosity during KBr-KCl replacement as an analogue for fluid-rock interactions in natural systems. By performing operando 4D synchrotron tomography, coupled with deep learning-based image processing and a set of characterisation tools (e.g., SMDs and MFs), we were able to evaluate the structural and morphological properties of the induced pore space.

Our findings indicate that complex relationships exist between dissolution and precipitation processes, dominant transport regimes, and effective transport properties (e.g., local permeability), with the relationships evolving over time. These complex interrelationships cannot be effectively described by only total porosity but require quantifying the evolution of the pore structure and morphology. We employ a set of SMDs and MFs and show that they can effectively elucidate the evolution of pore structures and their interdependent dynamics with transport regimes, dissolution and precipitation processes, and effective transport properties. Using these tools, we could identify three stages during our KBr-KCl replacement experiments, including an initial rapid evolution, transition stage, and steady state, marking a change in the transport regime from advective transport in the rapid evolution stage to more diffusion-driven transport in the last steady-state stage. Furthermore, the contribution that each aspect of pore properties makes to the local permeability varies during each stage, as shown by our correlation analysis.

Altogether, our study indicates that, despite all the complexities involved, a comprehensive spatio-temporal characterisation of pore space using SMDs and MFs carries a lot of quantitative information about the evolution of pore structures and their impact on transport properties. This suggests that incorporating these characterisation tools in an integrated reactive transport model can improve the predictive capabilities of these models. Although our findings may not be extrapolated to all mineral replacement reactions, some generalisations may be drawn to replacements involving epitaxial growth because it appears to play an important role in the evolution of pore structures. However, additional experiments are needed on other mineral replacements under relevant pressures and temperatures to establish and constrain the relationships between the pore structures and effective transport properties.

Conflict of Interest Statement

The authors have no conflicts of interest to disclose.

Open Research Section

Data availability statement

The dataset used in this study is available at Amiri (2025a). The code for characterising the microstructures using SMDs is provided in Amiri (2025b). Supplementary videos and

the data required to reproduce the figures are accessible via the Yoda data repository at Utrecht University Amiri, Freitas, et al. (2024).

Acknowledgments

This research was supported by a European Research Council (ERC) starting grant "nanoEARTH" (#852069) awarded to O. Plümper. We also acknowledge Swiss Light Source, Paul Scherrer Institut (PSI) for their technical support and access to TOMCAT beamline where the KBr-KCl experiments were conducted. Some portions of the manuscript text were improved with the assistance of an AI language model (ChatGPT, developed by OpenAI) to enhance clarity and readability. The authors reviewed and verified all AI-assisted edits and take full responsibility for the content.

References

Ajdari, A., & Bocquet, L. (2006). Giant amplification of interfacially driven transport by hydrodynamic slip: Diffusio-osmosis and beyond. *Physical Review Letters*, *96*(18), 186102.

Amiri, H. (2025a). *Dataset for kbr-kcl replacement using operando synchrotron tomography experiments- part 1 [dataset].* https://doi.org/10.5281/zenodo.16875392. Zenodo. doi: 10.5281/zenodo.16875392

Amiri, H. (2025b). *hamediut/poreeditgan: Analysis scripts for kbr–kcl replacement experiments (version 1.0.0) [software].* https://doi.org/10.5281/zenodo.16926276. Zenodo. doi: 10.5281/zenodo.16926276

Amiri, H., Freitas, D., Rizzo, R., Chogani, A., Schlepütz, C., Fusseis, F., & Plümper, O. (2024). *Data publication for unveiling reaction-induced porosity evolution in mineral replacement reactions using time-resolved synchrotron x-ray tomography.* https://doi.org/10.24416/UU01-4S7L5C.

Amiri, H., Vogel, H., & Plümper, O. (2024). New 2d to 3d reconstruction of heterogeneous porous media via deep generative adversarial networks (GANs). *Journal of Geophysical Research: Machine Learning and Computation*, *1*(3), e2024JH000178.

Andreani, M., Luquot, L., Gouze, P., Godard, M., Hoise, E., & Gibert, B. (2009). Experimental study of carbon sequestration reactions controlled by the percolation of co2-rich brine through peridotites. *Environmental Science & Technology*, *43*(4), 1226–1231.

Andrew, M. (2018). A quantified study of segmentation techniques on synthetic geological xrm and fib-sem images. *Computational Geosciences*, *22*(6), 1503–1512.

Angiboust, S., Pettke, T., De Hoog, J. C., Caron, B., & Oncken, O. (2014). Channelized fluid flow and eclogite-facies metasomatism along the subduction shear zone. *Journal of Petrology*, *55*(5), 883–916.

Bach, W., Paulick, H., Garrido, C. J., Ildefonse, B., Meurer, W. P., & Humphris, S. E. (2006). Unraveling the sequence of serpentinization reactions: petrography, mineral chemistry, and petrophysics of serpentinites from mar 15 n (odp leg 209, site 1274). *Geophysical Research Letters*, *33*(13).

Beaudoin, N., Hamilton, A., Koehn, D., Shipton, Z. K., & Kelka, U. (2018). Reaction-induced porosity fingering: replacement dynamic and porosity evolution in the kbr-kcl system. *Geochimica et Cosmochimica Acta*, *232*, 163–180.

Berg, S., Kutra, D., Kroeger, T., Straehle, C. N., Kausler, B. X., Haubold, C., ... others (2019). Ilastik: interactive machine learning for (bio) image analysis. *Nature Methods*, *16*(12), 1226–1232.

Boelens, A. M., & Tchelepi, H. A. (2021). Quantimpy: Minkowski functionals and functions with python. *SoftwareX*, *16*, 100823.

Bostanabad, R., Zhang, Y., Li, X., Kearney, T., Brinson, L. C., Apley, D. W., ... Chen, W. (2018). Computational microstructure characterization and reconstruction: Review of

the state-of-the-art techniques. *Progress in Materials Science*, *95*, 1–41.

Breiman, L. (2001). Random forests. *Machine Learning*, *45*, 5–32.

Chen, P.-E., Raghavan, R., Zheng, Y., Li, H., Ankit, K., & Jiao, Y. (2022). Quantifying microstructural evolution via time-dependent reduced-dimension metrics based on hierarchical n-point polytope functions. *Physical Review E*, *105*(2), 025306.

Chen, P.-E., Xu, W., Chawla, N., Ren, Y., & Jiao, Y. (2019). Hierarchical n-point polytope functions for quantitative representation of complex heterogeneous materials and microstructural evolution. *Acta Materialia*, *179*, 317–327.

Da Wang, Y., Shabaninejad, M., Armstrong, R. T., & Mostaghimi, P. (2020). Physical accuracy of deep neural networks for 2d and 3d multi-mineral segmentation of rock micro-ct images. *arXiv preprint arXiv:2002.05322*.

Engvik, A. K., Putnis, A., Fitz Gerald, J. D., & Austrheim, H. (2008). Albitization of granitic rocks: the mechanism of replacement of oligoclase by albite. *The Canadian Mineralogist*, *46*(6), 1401–1415.

Fusseis, F., Steeb, H., Xiao, X., Zhu, W.-l., Butler, I. B., Elphick, S., & Mäder, U. (2014). A low-cost x-ray-transparent experimental cell for synchrotron-based x-ray microtomography studies under geological reservoir conditions. *Journal of Synchrotron Radiation*, *21*(1), 251–253.

Gardner, J., Wheeler, J., & Mariani, E. (2021). Interactions between deformation and dissolution-precipitation reactions in plagioclase feldspar at greenschist facies. *Lithos*, *396*, 106241.

Hommel, J., Coltman, E., & Class, H. (2018). Porosity–permeability relations for evolving pore space: a review with a focus on (bio-) geochemically altered porous media. *Transport in Porous Media*, *124*(2), 589–629.

Iassonov, P., Gebrenegus, T., & Tuller, M. (2009). Segmentation of x-ray computed tomography images of porous materials: A crucial step for characterization and quantitative analysis of pore structures. *Water Resources Research*, *45*(9).

Jiao, Y., Stillinger, F., & Torquato, S. (2007). Modeling heterogeneous materials via two-point correlation functions: Basic principles. *Physical review E*, *76*(3), 031110.

Jiao, Y., Stillinger, F., & Torquato, S. (2008). Modeling heterogeneous materials via two-point correlation functions. ii. algorithmic details and applications. *Physical Review E*, *77*(3), 031135.

Jiao, Y., Stillinger, F., & Torquato, S. (2009). A superior descriptor of random textures and its predictive capacity. *Proceedings of the National Academy of Sciences*, *106*(42), 17634–17639.

Julia, M., Putnis, C. V., King, H. E., & Renard, F. (2023). Coupled dissolution-precipitation and growth processes on calcite, aragonite, and carrara marble exposed to cadmium-rich aqueous solutions. *Chemical Geology*, *621*, 121364.

Kaestner, A., Lehmann, E., & Stampanoni, M. (2008). Imaging and image processing in porous media research. *Advances in Water Resources*, *31*(9), 1174–1187.

Kar, A., Chiang, T.-Y., Ortiz Rivera, I., Sen, A., & Velegol, D. (2015). Enhanced transport into and out of dead-end pores. *ACS nano*, *9*(1), 746–753.

Kar, A., McEldrew, M., Stout, R. F., Mays, B. E., Khair, A., Velegol, D., & Gorski, C. A. (2016). Self-generated electrokinetic fluid flows during pseudomorphic mineral replacement reactions. *Langmuir*, *32*(21), 5233–5240.

Karimpouli, S., & Tahmasebi, P. (2019). Segmentation of digital rock images using deep convolutional autoencoder networks. *Computers & Geosciences*, *126*, 142–150.

Kasioptas, A., Perdikouri, C., Putnis, C., & Putnis, A. (2008). Pseudomorphic replacement of single calcium carbonate crystals by polycrystalline apatite. *Mineralogical Magazine*, *72*(1), 77–80.

Kaur, P., Chaudhri, N., Hofmann, A. W., Raczek, I., Okrusch, M., Skora, S., & Baumgartner, L. P. (2012). Two-stage, extreme albitization of a-type granites from rajasthan, nw india. *Journal of Petrology*, *53*(5), 919–948.

Kelemen, P. B., & Matter, J. (2008). In situ carbonation of peridotite for (CO_2) storage. *Proceedings of the National Academy of Sciences*, *105*(45), 17295–17300.

Koehn, D., Piazolo, S., Beaudoin, N. E., Kelka, U., Spruženiece, L., Putnis, C. V., & Toussaint, R. (2021). Relative rates of fluid advection, elemental diffusion and replacement govern reaction front patterns. *Earth and Planetary Science Letters*, *565*, 116950.

Kondratiuk, P., Tredak, H., Ladd, A. J., & Szymczak, P. (2015). Synchronization of dissolution and precipitation fronts during infiltration-driven replacement in porous rocks. *Geophysical Research Letters*, *42*(7), 2244–2252.

Kondratiuk, P., Tredak, H., Upadhyay, V., Ladd, A. J., & Szymczak, P. (2017). Instabilities and finger formation in replacement fronts driven by an oversaturated solution. *Journal of Geophysical Research: Solid Earth*, *122*(8), 5972–5991.

Lefeuvre, B., Beaudoin, N., Centrella, S., Le Gallais, T., Ducousso, M., & Callot, J.-P. (2024). Dynamic investigation of high-temperature dolomitization of polycrystalline carrara marble. *Chemical Geology*, *646*, 121901.

Lopes, P. C. F., Pereira, A. M. B., Clua, E. W. G., & Leiderman, R. (2022). A gpu implementation of the pcg method for large-scale image-based finite element analysis in heterogeneous periodic media. *Computer Methods in Applied Mechanics and Engineering*, *399*, 115276.

Lopes, P. C. F., Vianna, R. S., Sapucaia, V. W., Semeraro, F., Leiderman, R., & Pereira, A. M. (2023). Simulation toolkit for digital material characterization of large image-based microstructures. *Computational Materials Science*, *219*, 112021.

Lu, B., & Torquato, S. (1992). Lineal-path function for random heterogeneous materials. *Physical Review A*, *45*(2), 922.

Luhmann, A. J., Kong, X.-Z., Tutolo, B. M., Garapati, N., Bagley, B. C., Saar, M. O., & Seyfried Jr, W. E. (2014). Experimental dissolution of dolomite by CO_2-charged brine at 100 °C and 150 bar: Evolution of porosity, permeability, and reactive surface area. *Chemical Geology*, *380*, 145–160.

Malvoisin, B., Podladchikov, Y. Y., & Myasnikov, A. V. (2021). Achieving complete reaction while the solid volume increases: A numerical model applied to serpentinisation. *Earth and Planetary Science Letters*, *563*, 116859.

Marone, F., Schlepütz, C. M., Marti, S., Fusseis, F., Velásquez-Parra, A., Griffa, M., ... Stampanoni, M. (2020). Time resolved in situ x-ray tomographic microscopy unraveling dynamic processes in geologic systems. *Frontiers in Earth Science*, *7*, 346.

Marone, F., Studer, A., Billich, H., Sala, L., & Stampanoni, M. (2017). Towards on-the-fly data post-processing for real-time tomographic imaging at tomcat. *Advanced Structural and Chemical Imaging*, *3*(1), 1–11.

Mecke, K. (1998). Integral geometry in statistical physics. *International Journal of Modern Physics B*, *12*(09), 861–899.

Mecke, K. (2000). Additivity, convexity, and beyond: applications of minkowski functionals in statistical physics. In *Statistical physics and spatial statistics: The art of analyzing and modeling spatial structures and pattern formation* (pp. 111–184). Springer.

Mecke, K., & Arns, C. (2005). Fluids in porous media: a morphometric approach. *Journal of Physics: Condensed Matter*, *17*(9), S503.

Menke, H., Andrew, M., Blunt, M., & Bijeljic, B. (2016). Reservoir condition imaging of reactive transport in heterogeneous carbonates using fast synchrotron tomography—effect of initial pore structure and flow conditions. *Chemical Geology*, *428*, 15–26.

Min, T., Gao, Y., Chen, L., Kang, Q., & Tao, W.-w. (2016). Changes in porosity, permeability and surface area during rock dissolution: Effects of mineralogical heterogeneity. *International Journal of Heat and Mass Transfer*, *103*, 900–913.

Mosser, L., Dubrule, O., & Blunt, M. J. (2017). Reconstruction of three-dimensional porous media using generative adversarial neural networks. *Physical Review E*, *96*(4), 043309.

Musy, M., Jacquenot, G., Dalmasso, G., de Bruin, R., neoglez, Müller, J., ... Schneider, O. (2022, August). *marcomusy/vedo: 2022.3.0.* Zenodo. Retrieved from `https://doi.org/10.5281/zenodo.7019968` doi: 10.5281/zenodo.7019968

Niu, Y., Mostaghimi, P., Shabaninejad, M., Swietojanski, P., & Armstrong, R. T. (2020).

Digital rock segmentation for petrophysical analysis with reduced user bias using convolutional neural networks. *Water Resources Research*, *56*(2), e2019WR026597.

Noiriel, C., Oursin, M., & Daval, D. (2020). Examination of crystal dissolution in 3D: A way to reconcile dissolution rates in the laboratory? *Geochimica et Cosmochimica Acta*, *273*, 1–25.

Noiriel, C., & Renard, F. (2022). Four-dimensional x-ray micro-tomography imaging of dynamic processes in geosciences. *Comptes Rendus. Géoscience*, *354*(G2), 255–280.

Norberg, N., Neusser, G., Wirth, R., & Harlov, D. (2011). Microstructural evolution during experimental albitization of k-rich alkali feldspar. *Contributions to Mineralogy and Petrology*, *162*(3), 531–546.

Pearson, K. (1896). Vii. mathematical contributions to the theory of evolution.—iii. regression, heredity, and panmixia. *Philosophical Transactions of the Royal Society of London. Series A, containing papers of a mathematical or physical character*(187), 253–318.

Pedrosa, E., Putnis, C., Renard, F., Burgos-Cara, A., Laurich, B., & Putnis, A. (2016a). Porosity generated during the fluid-mediated replacement of calcite by fluorite. *CrystEngComm*, *18*(36), 6867–6874.

Pedrosa, E., Putnis, C. V., & Putnis, A. (2016b). The pseudomorphic replacement of marble by apatite: The role of fluid composition. *Chemical Geology*, *425*, 1–11.

Perdikouri, C., Kasioptas, A., Geisler, T., Schmidt, B. C., & Putnis, A. (2011). Experimental study of the aragonite to calcite transition in aqueous solution. *Geochimica et Cosmochimica Acta*, *75*(20), 6211–6224.

Plümper, O., Botan, A., Los, C., Liu, Y., Malthe-Sørenssen, A., & Jamtveit, B. (2017a). *Fluid-driven metamorphism of the continental crust governed by nanoscale fluid flow. nat geosci 10: 685–690.*

Plümper, O., Botan, A., Los, C., Liu, Y., Malthe-Sørenssen, A., & Jamtveit, B. (2017c). Fluid-driven metamorphism of the continental crust governed by nanoscale fluid flow. *Nature Geoscience*, *10*(9), 685–690.

Plümper, O., John, T., Podladchikov, Y. Y., Vrijmoed, J. C., & Scambelluri, M. (2017b). Fluid escape from subduction zones controlled by channel-forming reactive porosity. *Nature Geoscience*, *10*(2), 150–156.

Plümper, O., Røyne, A., Magrasó, A., & Jamtveit, B. (2012). The interface-scale mechanism of reaction-induced fracturing during serpentinization. *Geology*, *40*(12), 1103–1106.

Pollok, K., Lloyd, G. E., Austrheim, H., & Putnis, A. (2008). Complex replacement patterns in garnets from bergen arcs eclogites: a combined ebsd and analytical tem study. *Geochemistry*, *68*(2), 177–191.

Poonoosamy, J., Wanner, C., Alt Epping, P., Águila, J., Samper, J., Montenegro, L., ... others (2021). Benchmarking of reactive transport codes for 2D simulations with mineral dissolution–precipitation reactions and feedback on transport parameters. *Computational Geosciences*, *25*, 1337–1358.

Putnis, A. (2009). Mineral replacement reactions. *Reviews in mineralogy and geochemistry*, *70*(1), 87–124.

Putnis, A. (2015). Transient porosity resulting from fluid–mineral interaction and its consequences. *Reviews in Mineralogy and Geochemistry*, *80*(1), 1–23.

Putnis, C. V., & Mezger, K. (2004). A mechanism of mineral replacement: isotope tracing in the model system KCl-KBr-H_2O. *Geochimica et Cosmochimica Acta*, *68*(13), 2839–2848.

Putnis, C. V., Tsukamoto, K., & Nishimura, Y. (2005). Direct observations of pseudomorphism: compositional and textural evolution at a fluid-solid interface. *American Mineralogist*, *90*(11-12), 1909–1912.

Raufaste, C., Jamtveit, B., John, T., Meakin, P., & Dysthe, D. K. (2011). The mechanism of porosity formation during solvent-mediated phase transformations. *Proceedings of the Royal Society A: Mathematical, Physical and Engineering Sciences*, *467*(2129), 1408–1426.

Ray, N., Rupp, A., Schulz, R., & Knabner, P. (2018). Old and new approaches predicting the diffusion in porous media. *Transport in Porous Media*, *124*, 803–824.

Rizzo, R. E., Freitas, D., Gilgannon, J., Seth, S., Butler, I. B., McGill, G. E., & Fusseis, F. (2024). Using internal standards in time-resolved x-ray micro-computed tomography to quantify grain-scale developments in solid-state mineral reactions. *Solid Earth*, *15*(4), 493–512.

Rodgers, J. L., & Nicewander, W. A. (1988). Thirteen ways to look at the correlation coefficient. *The American Statistician*, *42*(1), 59–66.

Ronneberger, O., Fischer, P., & Brox, T. (2015). U-net: Convolutional networks for biomedical image segmentation. In *International conference on medical image computing and computer-assisted intervention* (pp. 234–241).

Smith, M. M., Sholokhova, Y., Hao, Y., & Carroll, S. A. (2013). CO_2-induced dissolution of low permeability carbonates. part i: Characterization and experiments. *Advances in Water Resources*, *62*, 370–387.

Steefel, C. I., Beckingham, L. E., & Landrot, G. (2015). Micro-continuum approaches for modeling pore-scale geochemical processes. *Reviews in Mineralogy and Geochemistry*, *80*(1), 217–246.

Szymczak, P., & Ladd, A. J. (2014). Reactive-infiltration instabilities in rocks. part 2. dissolution of a porous matrix. *Journal of Fluid Mechanics*, *738*, 591–630.

Tartakovsky, A. M., Meakin, P., Scheibe, T. D., & Wood, B. D. (2007). A smoothed particle hydrodynamics model for reactive transport and mineral precipitation in porous and fractured porous media. *Water Resources Research*, *43*(5).

Thevenaz, P., Ruttimann, U. E., & Unser, M. (1998). A pyramid approach to subpixel registration based on intensity. *IEEE transactions on image processing*, *7*(1), 27–41.

Torquato, S., & Haslach, H. (2002). Random heterogeneous materials: microstructure and macroscopic properties. *Appl. Mech. Rev.*, *55*(4), B62–B63.

Varfolomeev, I., Yakimchuk, I., & Safonov, I. (2019). An application of deep neural networks for segmentation of microtomographic images of rock samples. *Computers*, *8*(4), 72.

Vogel, H.-J., Weller, U., & Schlüter, S. (2010). Quantification of soil structure based on minkowski functions. *Computers & Geosciences*, *36*(10), 1236–1245.

Wang, X., Li, X.-H., Cho, J. W., Russ, B. E., Rajamani, N., Omelchenko, A., ... others (2021). U-net model for brain extraction: Trained on humans for transfer to non-human primates. *Neuroimage*, *235*, 118001.

Weber, J., Cheshire, M. C., Bleuel, M., Mildner, D., Chang, Y.-J., Ievlev, A., ... Anovitz, L. M. (2021). Influence of microstructure on replacement and porosity generation during experimental dolomitization of limestones. *Geochimica et Cosmochimica Acta*, *303*, 137–158.

Weber, J., Starchenko, V., Ilavsky, J., Allard, L. F., Mata, J., Debeer-Schmitt, L., ... others (2023). Grain boundary widening controls siderite ($FeCO_3$) replacement of limestone ($CaCO_3$). *Scientific Reports*, *13*(1), 4581.

Wildenschild, D., & Sheppard, A. P. (2013). X-ray imaging and analysis techniques for quantifying pore-scale structure and processes in subsurface porous medium systems. *Advances in Water Resources*, *51*, 217–246.

Xie, M., Mayer, K. U., Claret, F., Alt-Epping, P., Jacques, D., Steefel, C., ... Simunek, J. (2015). Implementation and evaluation of permeability-porosity and tortuosity-porosity relationships linked to mineral dissolution-precipitation. *Computational Geosciences*, *19*, 655–671.

Yarushina, V. M., Podladchikov, Y. Y., & Vershinin, A. V. (2025). A micromechanical model for mineral replacement reactions and associated deformation: From pore clogging to solid volume increase. *American Journal of Science*, *325*, Arcicle–11.